



# Retrieved Thermodynamic Structure of Hurricane Rita (2005) from

## Airborne Multi-Doppler Radar Data

Annette M. Boehm \* †

*Department of Atmospheric Sciences, University of Hawai‘i at Mānoa, Honolulu, HI*

Michael M. Bell

*Department of Atmospheric Science, Colorado State University, Fort Collins, CO*

\*Corresponding author: Annette Boehm, foerster@hawaii.edu

†Current Affiliation: Meteorologisches Observatorium Hohenpeissenberg, Deutscher Wetterdienst, Hohenpeissenberg, Germany

## ABSTRACT

The newly developed SAMURAI-TR is used to estimate three-dimensional temperature and pressure perturbations in Hurricane Rita on 23 September 2005 from multi-Doppler radar data during the RAINEX field campaign. These are believed to be the first fully three-dimensional gridded thermodynamic observations from a TC. Rita was a major hurricane at this time and was affected by  $13 \text{ m s}^{-1}$  deep-layer vertical wind shear. Analysis of the contributions of the kinematic and retrieved thermodynamic fields to different azimuthal wavenumbers suggests the interpretation of eyewall convective forcing within a three-level framework of balanced, quasi-balanced, and unbalanced motions. The axisymmetric, wavenumber-0 structure was approximately in thermal-wind balance, resulting in a large pressure drop and temperature increase toward the center. The wavenumber-1 structure was determined by the interaction of the storm with environmental vertical wind shear resulting in a quasi-balance between shear and shear-induced kinematic and thermodynamic perturbations. The observed wavenumber-1 thermodynamic asymmetries corroborate results of previous studies on the response of a vortex tilted by shear, and add new evidence that the vertical motion is nearly hydrostatic on the wavenumber-1 scale. Higher-order wavenumbers were associated with unbalanced motions and convective cells within the eyewall. The unbalanced vertical acceleration was positively correlated with buoyant forcing from thermal perturbations and negatively correlated with perturbation pressure gradients relative to the balanced vortex.

## 1. Introduction

Tropical cyclone (TC) intensity change remains a challenging forecast problem (DeMaria et al. 2014; Trabing and Bell 2020). An improved understanding of the impacts of environmental factors on the internal structure of TCs, and the mechanisms by which convective activity and organization affect intensity change are instrumental in improving our forecast capability.

Vertical wind shear (VWS) is one of the primary environmental factors directly impacting the eyewall structure. Many observational studies, including composite studies of satellite-derived precipitation data (Hence and Houze 2011), airborne radar data (Marks et al. 1992; Black et al. 2002; Reasor and Eastin 2012; Reasor et al. 2013; DeHart et al. 2014), and lightning data (Corbosiero and Molinari 2002, 2003) have found a shear-induced wavenumber-1 pattern in the convective structure of the eyewall, with the strongest upward motion located predominantly downshear and the highest radar reflectivities left of shear. Black et al. (2002) and Braun et al. (2006) highlight that while the time-averaged vertical motion shows a clear wavenumber-1 pattern, the instantaneous vertical motion is closely linked to individual deep updraft towers, which typically form downshear, mature as they rotate cyclonically around the eyewall, and dissipate right-of-shear. The time-averaged wavenumber-1 pattern represents the envelope of these convective elements.

Jones (1995) investigated the impacts of VWS on barotropic vortices and found that the vortex initially tilts downshear, then precesses and eventually reaches an equilibrium tilt direction in the left of shear semicircle. The tilt introduces anomalies in potential temperature and vertical velocity such that the flow remains balanced. However, the effects of diabatic heating were not included in that study as the vortex was dry and barotropic. The potential temperature and vertical velocity anomalies were found to be phase-shifted by  $90^\circ$ , with adiabatic ascent right-of-tilt, negative potential temperature anomalies downtilt, adiabatic descent left-of-tilt, and positive

potential temperature anomalies in the up tilt direction. This pattern is consistent with lifting along isentropes right-of-tilt, resulting in negative potential temperature anomalies downshear, and adiabatic descent left-of-tilt, resulting in positive potential temperature anomalies upshear.

Frank and Ritchie (1999) investigated the impact of VWS on the location of forced ascent in the eyewall with a series of dry and moist simulations using a full physics model. In their dry simulations, and in the early periods of their moist simulations, the downshear right direction is the preferred location for strong, deep ascent, whereas the downshear left is favored later in the moist simulations. They conclude that adiabatic lifting mechanisms dominate in the dry and early moist simulations, but once the eyewall becomes saturated the latent heat release interrupts the adiabatic lifting mechanisms.

A quasi-steady orientation of the tilt toward the downshear left direction was also found in studies by Wang and Holland (1996) and Reasor et al. (2004). Reasor et al. (2004), however, questioned the role of the diabatically driven secondary circulation to realign the vortex. They argue that the realignment is primarily due to dry adiabatic dynamics, specifically the damping of vortex Rossby waves associated with the tilt asymmetry. The diabatically driven secondary circulation is believed to play only an indirect role with its axisymmetric component acting to increase the damping efficiency.

Reasor and Eastin (2012) found wavenumber-1 asymmetries in vertically-sheared Hurricane Guillermo (1997) for two different intensive observing periods (IOPs). Their airborne Doppler radar observations showed wavenumber-1 vertical velocity asymmetries at 5 km altitude, with the largest upward motion downshear left. Wavenumber-1 vertical vorticity asymmetries were evident at 2 km altitude, with positive vorticity left-of-shear out to 20 km radius and negative vorticity beyond 30 km radius. They suggested that the vorticity structure can be attributed to vortex tube stretching and the large-scale tilt of the vortex.

The majority of studies addressing the impact of VWS on eyewall convection have focused on the wavenumber-1 structure of wind and precipitation fields. Less attention has been paid to the thermodynamic properties, in part because of a lack of observations. Jones (1995) showed that the tilt introduces a thermal couplet. She also mentioned that horizontal advection may act to rotate the thermal anomalies cyclonically with height, whereas vertical advection may act to rotate the thermal anomalies anticyclonically. In a subsequent study with baroclinic vortices, Jones (2000) found an anticyclonic rotation of the temperature anomalies with height and attributed it to the coincident anticyclonic rotation of the tilt with height, keeping the relative orientation of tilt and temperature anomalies constant. She also showed that the temperature anomalies resulted in enhanced low-level stability uptilt, and reduced low-level stability downtilt.

Reasor and Eastin (2012) derived potential temperature asymmetries from aircraft flight-level measurements of Hurricane Guillermo (1997) for two different IOPs and two vertical levels, 3 km and 6 km. Cold anomalies were located left-of-shear at 3 km for both of their IOPs, and left-of-shear and downshear respectively at 6 km. Their data coverage is limited, but their results are in agreement with Jones (2000), showing a mesoscale thermal couplet, with cold anomalies in the downtilt direction. Braun et al. (2006) found a similar relationship between tilt and potential temperature anomalies in their high-resolution simulation of Hurricane Bonnie, with cold anomalies located in the downtilt direction at 5 km height. They argue that the convective forcing caused by this temperature couplet is weak and only plays a minor role in forcing eyewall convection. Our paper will expand on these studies by using a new radar-based thermodynamic retrieval technique to document the observed three-dimensional thermodynamic structure of Hurricane Rita (2005) while it was under the impact of VWS.

Axisymmetric conceptual and numerical models of the eyewall are characterized by moist neutral ascent forced by boundary layer convergence. The eyewall is pictured as a ring of mesoscale ascent, with air parcels rising along constant angular momentum surfaces at the speed they obtain leaving the boundary layer (Emanuel 1995). In contrast, three-dimensional models suggest that a significant fraction of eyewall convective elements may contain positive buoyancy, with a large fraction of the upward mass transport being accomplished by a few buoyant undilute updrafts (Braun et al. 2006). Observational data sets are necessary to investigate the respective dynamic and thermodynamic contributions to convective forcing in the eyewall.

Recent observational studies (Guimond et al. 2010, 2016; Rogers et al. 2015, 2020; Fischer et al. 2020) suggest that an improved understanding of the processes that determine the location and strength of convection might improve the ability to forecast TC intensity change. Idealized studies by Pendergrass and Willoughby (2009) and Willoughby (2009) used the classical Sawyer-Eliassen equation in height coordinates to study the effects of radial location and longevity of convective cells. They showed that the intensification efficiency caused by heating in the eyewall critically depends on the location and timing of these convective cells. The intensification efficiency increases with decreased distance to the center, and with increased duration. Vigh and Schubert (2009) used a theoretical model to analyze the conditions under which a TC can rapidly develop a warm core. They emphasize the role of inertial stability for the intensification efficiency, with high intensification efficiencies in the high-inertial-stability region inside the radius of maximum wind (RMW) and low intensification efficiencies in the low-inertial-stability region outside the RMW. Airborne radar (Rogers et al. 2013) and flight level (Martinez et al. 2017) data provide observational support for the prior theoretical and numerical studies, with the presence of convective bursts and a ring of vorticity consistently located inside the radius of maximum wind more frequently than in steady-state or weakening storms.

Two modeling studies (Zhang et al. 2000; Braun 2002) and one observational study (Eastin et al. 2005a) investigated the buoyancy of convective vertical motion in the eyewall of TCs. The studies came to different conclusions. Individual updrafts can be vertically accelerated by vertical perturbation pressure gradients and buoyancy:

$$\frac{Dw}{Dt} = -\frac{1}{\rho} \frac{\partial p}{\partial z} - g = -\frac{1}{\rho} \frac{\partial p'}{\partial z} - g \frac{\rho'}{\rho_0} \quad (1)$$

where  $w$  is the vertical velocity,  $D/Dt$  the material derivative,  $p$  the pressure,  $\rho$  the density,  $g$  the gravitational acceleration, and  $z$  the height. Primes represent the differences between an air parcel and a reference state, e.g.  $\rho' = \rho_p - \rho_0$ . While Zhang et al. (2000) found that the eyewall is negatively buoyant and the updrafts are driven mainly by the vertical perturbation pressure gradient force, Braun (2002) and Eastin et al. (2005a) found areas of positive buoyancy in the eyewall. Smith et al. (2005) addressed these seemingly contradicting findings by pointing out the importance of the definition of the reference state for the interpretation of the results. While the sum of the two forcing terms is unique, their partition is determined by the prescribed reference state that is crucial for the interpretation.

Axisymmetric TCs are usually considered to be in approximate hydrostatic balance, and in approximate gradient wind balance outside the boundary layer. Based on in-situ aircraft observations, Willoughby (1990) showed that the gradient wind balance is valid to within  $1.5 \text{ m s}^{-1}$  above the boundary layer for the azimuthal mean tangential wind. The gradient balance condition indicates that the bulk of the pressure gradient field is in balance with the primary wind field and does not act to accelerate air parcels radially. The hydrostatic assumption is valid if vertical accelerations are negligible, which is the case for convectively-neutral updrafts. This hydrostatic assumption might not be valid for individual updrafts, but it is valid on average for the primary vortex. Hence, using the thermal wind balanced vortex as the reference state for buoyancy calculations is the natural

choice for TCs (Smith et al. 2005), and makes interpretation easier. In this framework positive buoyancy translates into upward acceleration, unless the vertical perturbation pressure gradient counteracts. This upward acceleration strengthens the secondary circulation, which in turn can enhance the primary circulation and thus intensify the TC.

Following this prior research, in the current study we seek to address the following science questions using field observations:

1. What are the mesoscale and convective-scale structures of the thermodynamic fields in the eyewall region?
2. How does vertical wind shear impact the thermodynamic structure?
3. Is the eyewall convectively buoyant?

Addressing these questions requires high-resolution kinematic and thermodynamic measurements. Measurements of the wind field throughout the entire vortex are necessary to compute the balanced vortex reference state, along with temperature, pressure and moisture measurements to determine whether or not a given eyewall location is buoyant. However, in-situ observations exist only along flight tracks or dropsonde paths. Hence, a complete picture of the three-dimensional distributions of buoyancy and pressure perturbations within the eyewall can't be obtained from direct observations.

In the past, several approaches have been taken to estimate pressure and temperature fields from radar data. Radar data are an excellent data source because they provide great spatial coverage at a good horizontal and vertical resolution. The traditional thermodynamic retrievals are based on seminal work by Gal-Chen (1978) and use the horizontal and vertical momentum equations, sometimes complemented with the thermodynamic equation and other constraints,

to infer thermodynamic properties from kinematic measurements (Gal-Chen 1978; Roux 1985; Viltard and Roux 1998; Liou 2001).

Foerster and Bell (2017, FB17 hereafter) developed a new thermodynamic retrieval specifically tailored toward TCs, called SAMURAI-TR (Spline Analysis at Mesoscale Utilizing Radar and Aircraft Instrumentation - Thermodynamic Retrieval). This new retrieval technique advances previous techniques in two key ways. First, SAMURAI-TR allows for use of the thermal wind balanced vortex reference state for buoyancy calculations, which both improves the numerical accuracy of the retrieval and facilitates the interpretation of the retrieved thermodynamic perturbations in TCs. Second, SAMURAI-TR builds on technical advancements from the recently developed variational wind retrieval software tool SAMURAI (Bell et al. 2012a; Foerster et al. 2014) that uses a spline-based representation of the retrieved variables. This spline representation provides analytic spatial derivatives that allow for specification of the three-dimensional pressure and temperature gradients as pseudo-observations from Doppler-derived winds and natural low-pass filtering capabilities. FB17's evaluation of SAMURAI-TR with a Weather Research and Forecasting (WRF) simulation of Hurricane Rita found the pressure retrieval to be accurate to within 0.25 hPa RMSE, and the temperature retrieval to within 0.7 K RMSE.

Here we apply the thermodynamic retrieval SAMURAI-TR to examine the observed kinematic and thermodynamic structure of Hurricane Rita (2005). In particular we focus on the effect of VWS on the thermodynamic structure of the eyewall convection, and the links between vertical motion and dynamic and thermodynamic forcing. Hurricane Rita provides an excellent dataset to study the mesoscale structure of a TC impacted by VWS. It is one of the most well observed storms in history, simultaneously observed by three different aircraft over an extended period of time during the Hurricane Rainband and Intensity Change Experiment (RAINEX, Houze et al. (2006)).

Section 2 describes the data and methods used in this study. Section 3 analyzes the kinematic and thermodynamic structure of Hurricane Rita on 23 September 2005, Section 4 investigates the contributions of the retrieved temperature and pressure fields to different azimuthal wavenumbers, and Section 5 summarizes the results and provides conclusions.

## 2. Data and Methods

### a. Hurricane Rita

Hurricane Rita was first classified as a tropical depression at 0000 UTC 18 September 2005 located north of the Dominican Republic, and intensified to tropical storm strength within the next 18 hours (Fig. 1). Rita moved northwestward and first strengthened slowly as it approached the Florida Straits, and then strengthened more rapidly afterwards over the very warm waters (near 30° C) of the Gulf of Mexico (Bell et al. 2012b). Within 36 hours, Rita had strengthened from tropical storm to Category-5 status at 1800 UTC 21 September. The TC reached an estimated peak intensity of 155 kts and minimum central pressure of 897 hPa at 0300 UTC 22 September, before weakening due to structural changes on 22 September, and increased VWS and slightly cooler waters on 23 September (Beven et al. 2008). Rita made landfall at 0740 UTC 24 September in southwestern Louisiana as a Category-3 Hurricane with an estimated intensity of 100 kts. One of the largest evacuations in U. S. history was conducted in anticipation of Rita's landfall. The storm surge that accompanied Rita devastated entire communities in coastal areas of southwestern Louisiana, and was estimated to be as high as 15 feet. Downed trees and power lines left well over one million customers without power for days and even weeks. Seven direct fatalities were reported. The total damage of Rita is estimated at about \$12 billion (NHC TC Report; Knabb et al. (2011)).

Nearly the entire lifecycle of Hurricane Rita was observed in detail during RAINEX. Previous observational studies have focused on Rita's structure during rapid intensification on 21 September and an eyewall replacement cycle on 22 September 2005. Didlake and Houze (2013a,b) documented the structure of the convective and stratiform sectors of the rainbands of Hurricane Rita on 21 September 2005. Bell et al. (2012b) examined the symmetric evolution of the hurricane as it underwent eyewall replacement, and Didlake and Houze (2011) analyzed the kinematics of the secondary eyewall on 22 September 2005. Guimond et al. (2018) examined the evolution of the eyewall replacement cycle from airborne radar with a focus on the boundary layer. The current study focuses on the structure of Hurricane Rita observed on 23 September 2005 when it weakened from a Category-4 to a Category-3 hurricane.

### *b. Observations*

RAINEX was the first experiment to use the high-resolution ELectrta DOppler RADar (ELDORA) in TCs, and the first experiment to simultaneously use three airborne dual-Doppler radars. The Naval Research Laboratory (NRL) P-3 with ELDORA, and the two NOAA P-3s (denoted N42 and N43) each had dual-Doppler capability that allowed for excellent multi-Doppler geometry. The three P-3 aircraft sampled Rita simultaneously (Fig. 1c), and the data used in this study were collected during a period of 132 minutes from 2022 UTC to 2235 UTC. ‘Figure-four’ flight patterns (N43) were combined with circumnavigations (NRL) and low-altitude eyewall crossings (N42) to collect complementary data sets, providing an excellent combination of data for Doppler wind synthesis. Since the flight tracks of the 3 aircraft were non-standard and could not be clearly divided into separate center passes, we divided the analysis into four consecutive periods of approximately 30 minutes each. Each 30 minute period contains enough data to provide a complete view of the entire eyewall, and corresponds roughly to one complete circumnavigation

of the eyewall by the NRL P-3. The first period lasts from 2022 to 2100 UTC, the second period from 2100 to 2130 UTC, the third period from 2130 to 2200 UTC, and the last period from 2200 to 2235 UTC. From now on, the different periods will be referred to by their respective reference times (2040 UTC, 2110 UTC, 2140 UTC, and 2210 UTC), where the storm's center position at reference time is used to define the center position of the respective analysis domain.

The main data source for all four periods is airborne radar data. A total of 6696 radar 'sweep' files, each corresponding to a 360-degree scan of the tail Doppler radar were used in the analyses (4810 NRL, 1000 N42, 886 N43), and were augmented by dropsonde data and flight level data from the two NOAA aircraft. The wind solution is dominated by the voluminous radar data, and is qualitatively similar without including the in-situ or atmospheric motion vectors.

Each radar sweep file was quality controlled before being used for multi-Doppler synthesis. First, navigation corrections were applied to correct for biases in the recorded aircraft position and orientation. The navigation corrections were estimated using a new method (Cai et al. 2015), which generalizes the previous methods of Testud et al. (1995), Georgis et al. (2000), and Bosart et al. (2002). The method uses surface echoes and near-aircraft echoes (when available) recorded during a straight and level calibration flight leg to assess the errors in the aircraft inertial navigation system. Second, an automatic editing script (Bell et al. 2013) was applied to remove the majority of the non-weather data, such as ground clutter, radar side lobes, and low signal-to-noise echoes. The script dealiased the Doppler velocity using a Bargin-Brown algorithm (Bargin and Brown 1980). Additional manual editing was performed to remove any remaining non-weather echoes and fix any dealiasing errors.

### *c. Retrieval*

The detailed method for retrieving 3D winds and thermodynamic structure of a TC from radar data is described and evaluated in Foerster (2016) and FB17, and is summarized briefly here. The retrieval of the thermodynamic structure of Hurricane Rita is performed in three distinct steps. The first step is to combine the radar data and complementary in-situ flight track, dropsonde and satellite atmospheric-motion-vector observations into a gridded SAMURAI mesoscale analysis. A domain size of 150 km x 150 km x 15 km is used in this study, with a horizontal resolution of 1 km and a vertical resolution of 0.5 km. The SAMURAI analysis is performed in two iterations, using larger low-pass filters ( $\sim 10 \delta x$ ) in the first iteration and smaller filters ( $\sim 2\delta x$ ) in the second iteration to obtain a mesoscale analysis. The  $\sim 2$ -km effective horizontal resolution is appropriate for the combined along-track resolution of 500 m for ELDORA and 1.5 km for the NOAA radars, and  $\sim 2$ -degree beamwidth of all the tail radars. A hybrid variational setting was used, limiting the elevation angle to 45° and neglecting the projection of the vertical wind in the Doppler velocity (Jorgensen et al. 1996; Foerster et al. 2014). The uncertainty in the retrieved wind field depends primarily on the geometry of the multiple airborne radar viewing angles, the amount of low-pass filtering, and the prescribed uncertainty of the observations. The spline analysis does not require interpolation or averaging of the unevenly distributed data to a uniform grid as in classical multi-Doppler synthesis, but instead variationally minimizes the difference between the analyzed wind directly at the observation location and the projected radial velocity or in situ measurement. The variational solution then represents the most likely state of the atmosphere given all of the available observations subject to the low-pass filtering constraint and prescribed errors. We estimate the wind uncertainty to be less than  $2 \text{ m s}^{-1}$  based on geometric considerations (Hildebrand et al.

1996) and statistical analysis of the difference between the synthesized wind and observations (not shown).

The second step of the retrieval method is to calculate the temperature and pressure fields,  $\bar{T}(r,z)$  and  $\bar{p}(r,z)$ , that balance the azimuthally-averaged radar-derived wind field using the thermal wind equation.  $\bar{T}(r,z)$  and  $\bar{p}(r,z)$  are then used as input for the pressure and temperature retrieval SAMURAI-TR. To compute the azimuthal average of the wind field, the center of the TC has to be determined. This is done by maximizing the circulation at the RMW at each vertical level, similar to the method of Marks et al. (1992). The mean center of the storm is defined as the average location of the centers between 2 km and 8 km altitude. The inward integration of the thermal wind equation (Smith 2006) is then used to calculate the azimuthal mean temperature and pressure field that balances the mean tangential wind field. The calculation is limited to altitudes above 2 km due to uncertainties in the balance approximation below that level where unbalanced frictional effects become important. The temperature and pressure profiles used to anchor the balanced vortex calculation are derived from the azimuthally-averaged SAMURAI analyzed temperature and pressure field at a radius of 60 km. The gaps in data coverage are either small enough or located favorably to not significantly affect the reference state calculation. The coverage out to 60 km radius is sufficient to calculate an average tangential wind speed, although a slight bias might be introduced because the data gaps are located predominantly towards the south. The data gap in the eye of Hurricane Rita at levels above 4 km prohibits calculation of the balanced pressure and temperature in that area. Fortunately, the thermal wind equation is integrated inwards and not outwards, therefore the data gap in the eye does not affect any other regions.

The third and final step of the method is the retrieval of the thermodynamic perturbations from the balanced reference state with SAMURAI-TR as described in FB17. The method solves for the perturbations of density potential temperature  $\theta'_\rho$  and non-dimensional pressure  $\pi'$  using a 3D

variational cost function. The retrieval consists of a set of five equations, two equations each for  $\theta'_\rho$  and  $\pi'$ , and one equation containing both variables. The exact equations <sup>1</sup> read:

$$\frac{1}{c_p \bar{\theta}_\rho} \left( \frac{\partial u}{\partial t} + u \frac{\partial u}{\partial x} + v \frac{\partial u}{\partial y} + w \frac{\partial u}{\partial z} - fv \right) + \frac{\partial \bar{\pi}}{\partial x} = A = -\frac{\partial \pi'}{\partial x} \quad (2)$$

$$\frac{1}{c_p \bar{\theta}_\rho} \left( \frac{\partial v}{\partial t} + u \frac{\partial v}{\partial x} + v \frac{\partial v}{\partial y} + w \frac{\partial v}{\partial z} + fu \right) + \frac{\partial \bar{\pi}}{\partial y} = B = -\frac{\partial \pi'}{\partial y} \quad (3)$$

$$\frac{1}{c_p \bar{\theta}_\rho} \left( \frac{\partial w}{\partial t} + u \frac{\partial w}{\partial x} + v \frac{\partial w}{\partial y} + w \frac{\partial w}{\partial z} \right) = C = -\frac{\partial \pi'}{\partial z} + \frac{g}{c_p \bar{\theta}_\rho^2} \theta'_\rho \quad (4)$$

$$\frac{-c_p \bar{\theta}_\rho^2}{g} \left( \frac{\partial A}{\partial z} - \frac{\partial C}{\partial x} \right) = D = \frac{\partial \theta'_\rho}{\partial x} - 2 \frac{\theta'_\rho}{\bar{\theta}_\rho} \frac{\partial \bar{\theta}_\rho}{\partial x} \quad (5)$$

$$\frac{-c_p \bar{\theta}_\rho^2}{g} \left( \frac{\partial B}{\partial z} - \frac{\partial C}{\partial y} \right) = E = \frac{\partial \theta'_\rho}{\partial y} - 2 \frac{\theta'_\rho}{\bar{\theta}_\rho} \frac{\partial \bar{\theta}_\rho}{\partial y} \quad (6)$$

where  $u$ ,  $v$ , and  $w$  denote the wind field components,  $f$  denotes the Coriolis parameter,  $c_p$  denotes the specific heat capacity at constant pressure,  $\bar{\pi}$  denotes the azimuthally averaged non-dimensional pressure, and  $\bar{\theta}_\rho$  denotes the azimuthally averaged density potential temperature. Analytic tests performed by FB17 indicate that SAMURAI-TR has good accuracy and can retrieve pressure to within 0.25 hPa and temperature to within 0.7 K RMSE.

### 3. Kinematic and Thermodynamic Structure of Hurricane Rita

The kinematic and thermodynamic structure of Hurricane Rita was investigated with respect to its variability over time, its response to VWS, and the characteristics of the eyewall convection.

Horizontal cross sections of radar reflectivity, horizontal wind, and vertical motion for the four analysis periods are shown in Figs. 2 and 3. The data coverage for all times is very good in the northern semicircle. Some gaps in coverage exist towards the southern edge of the domain and in the eye, which is in part due to the flight patterns and in part due to a lack of hydrometeors. The eyewall is located at a radius of around 25 km, containing the highest reflectivities and strongest

---

<sup>1</sup>We note that FB17 omitted the last term each in their retrieval equations 13 and 14, which can be neglected but is included here for completeness in the corresponding equations 5 and 6.

horizontal winds. All times show a consistent asymmetry related to VWS, with the largest radar reflectivities at all vertical levels in the northern part of the eyewall, which coincides with the left-of-shear semicircle. A detailed analysis of the shear is shown in Fig. 4 and described below. The largest vertical velocities are consistently in the eastern and northern part of the eyewall, whereas the western part shows predominantly downward motion. The largest maximum reflectivities occur at 2110 UTC, where the 40-dBZ surface extends above 5 km altitude. The vertical velocities in the northern part of the eyewall at 5 km altitude are collocated with the largest reflectivity values for 2140 UTC, and located radially inward of the largest reflectivity values for the other three times. Similar to what has been observed in several previous studies, new cells usually form in the downshear-right (here southeastern) part of the eyewall, mature as they rotate into the downshear-left (northern) part, and dissipate in the upshear-left (western) part of the eyewall.

The SAMURAI analyses were used to estimate storm motion, local shear, and the vertical tilt of the storm. As mentioned in section 2c, for each analysis time, the vortex center position was defined as the average of the center positions at the vertical levels from 2 km to 8 km altitude determined by maximizing the circulation at the RMW (Marks et al. 1992). The vortex center positions at the four consecutive times show the approximately linear, northwesterly track of Hurricane Rita during the observation period (Fig. 4, Table 1). Rita moved at a speed of  $5.3 \text{ m s}^{-1}$ , with a heading of  $321^\circ$ . The vortex tilted to the northeast during all four periods, with the tilt magnitude changing slightly from period to period. The tilt was defined as the difference between the center positions at 8 km and 2 km altitude.

The direction of the VWS was assessed using two different metrics, the local shear derived from the SAMURAI analyses and the large-scale SHIPS shear (Statistical Hurricane Intensity Prediction Scheme; DeMaria and Kaplan (1994)). The local shear was computed using the center-relative flow out to a radius of 40 km, which ensured sufficient data coverage for the shear calculation

except for the last period where the data gap to the south skews the results. Hence, the local shear is computed as the average of the results of the first three periods only where the center-relative flow for each vertical level was consistent over time. The deep-layer shear (12 km - 1.5 km) is  $13.0 \text{ m s}^{-1}$  in east-southeasterly direction ( $114^\circ$ ), and the shallow-layer shear (5 km - 1.5 km) is  $6.2 \text{ m s}^{-1}$  in easterly direction ( $92^\circ$ ). The large-scale shear was estimated using data from the SHIPS database. The shear values are averages between the SHIPS data for 1800 UTC 23 September and for 0000 UTC 24 September. The deep-layer shear (200-850 hPa) is  $12.3 \text{ m s}^{-1}$  to the north-northeast ( $22^\circ$ ), and the shallow-layer shear (500-850 hPa) is  $1.5 \text{ m s}^{-1}$  to the northeast ( $56^\circ$ ).

Data from sheared TCs are often analyzed with respect to the direction of the shear impacting them. However, in our case the two shear metrics show rather different results. Most notably, the deep-layer shear direction is different by over  $90^\circ$  from the local shear. Many studies that have analyzed the structure of sheared TCs (e.g. Jones 1995; Wang and Holland 1996; Reasor et al. 2004) found a quasi-steady orientation of the vortex tilt toward the downshear left, whereas, to the authors' knowledge, there is no study reporting a tilt toward the downshear right. Moreover, the largest radar reflectivities are usually found left of shear. We speculate that the discrepancy between the directions of the local and large-scale deep layer shear is due to the presence of a larger-scale trough near Rita, but the exact reasons for the difference are unclear. Since our results are much more consistent with previous work when analyzed with respect to the local shear direction, for the purposes of this study, the shear direction is defined as the direction of the local deep-layer shear ( $114^\circ$ ).

The SAMURAI analyses were transformed from Cartesian to cylindrical coordinates using the respective vortex center positions as points of origin. This transformation enables the computation of the azimuthally-averaged storm structure and the thermal wind balanced reference state (Fig. 5), as well as azimuthal wavenumber asymmetries presented later in the manuscript. Figures 5a-d

show maximum azimuthal mean tangential wind speeds in excess of  $50 \text{ m s}^{-1}$  at low levels at a radius of about 30 km during all four periods, and tangential wind speeds exceeding  $30 \text{ m s}^{-1}$  throughout the depth of the domain outside the RMW. The radial location of largest mean radar reflectivities ranges from about 25 km (2140 UTC) to about 32 km (2110 UTC). 2210 UTC exhibits an additional radar reflectivity maximum at large radii (around 55 km). At 2110 UTC and at 2210 UTC, the largest mean radar reflectivities are collocated with the largest tangential wind speeds.

Figures 5e-h show the balanced temperature increase ( $\bar{T}(r, z) - \bar{T}(r = 60 \text{ km}, z)$ ) and pressure drop ( $\bar{p}(r, z) - \bar{p}(r = 60 \text{ km}, z)$ ) from the edge of the domain toward the center of the storm, which were calculated using the mean tangential wind fields displayed in Figs. 5a-d. The pressure drop is most pronounced at lower levels, with a maximum pressure drop of  $\Delta p > 26 \text{ hPa}$  in all cases. The temperature increases towards the center, with a minimum at 4 km altitude and maximum from 6 to 9 km altitude. The maximum is subtle at 2110 UTC and more pronounced at 2040 UTC and 2210 UTC.

A subset of the retrieved perturbation pressure and temperature fields are shown in Figs. 6 and 7. The three-dimensional thermodynamic structure has been investigated extensively through numerical modeling (e.g. Jones 2000), but observational studies (e.g. Reasor and Eastin 2012) have been limited to a few flight levels and dropsonde profiles. We believe these to be the first fully three-dimensional gridded thermodynamic observations from a TC. The retrieved thermodynamic structures show evidence of a wavenumber-1 pattern with additional higher-order structure during all four periods (exemplified here by data at 5 km altitude, Fig. 6). Horizontal cross sections at different vertical levels (exemplified here by data at three different vertical levels at 2140 UTC, Fig. 7) show an azimuthal rotation of the patterns with height. To gain further insight into Rita's asymmetric structure the kinematic and thermodynamic variables are decomposed into azimuthal wavenumbers in the following section.

## 4. Azimuthal-Wavenumber Analysis

The SAMURAI analyses in cylindrical coordinates are used to compute a discrete one-dimensional Fourier transform for each radial annulus, with a radial spacing of 1-km and an azimuthal spacing of  $1^\circ$ . In case of missing data along a range ring the data were interpolated across the gap using one-dimensional cubic splines.

### a. Wavenumber-1 Structure: Shear

The horizontal cross sections of radar reflectivity and vertical velocity (Figs. 2 and 3) showed that the vertical velocity has an apparent wavenumber-1 component at mid-to-upper levels, with the strongest upward motion in the eastern and northern quadrants of the eyewall for all four periods. The wavenumber-1 patterns were similar for all four periods, such that only results for 2140 UTC will be shown herein (Fig. 8) for conciseness. The wavenumber-1 vertical velocity maximum is located in the northeastern eyewall between 20 and 35 km radius for all vertical levels (Fig. 8a), and the magnitude increases with height. No significant rotation of the vertical velocity with height is evident. The wavenumber-1 vorticity asymmetries (Fig. 8b) at 2 km look similar to the wavenumber-1 vorticity asymmetries in Hurricane Guillermo at 2 km (Reasor and Eastin 2012), with one dipole inside the RMW, and an oppositely oriented dipole outside. At 8 km, the convectively active region toward the northeast of the center is collocated with a region of positive vertical vorticity. This pattern might be attributed to vortex stretching in active convection.

As mentioned above, a novel aspect of this study is the unprecedented look at the thermodynamic fields of the entire vortex. The wavenumber-1 asymmetries of density potential temperature perturbations  $\theta'_\rho$  show a consistent picture over time. The anomalies are maximized around a radius of approximately 30 km, with the azimuthal orientation of the dipole similar for all radii (Fig. 8c). The cold anomalies at 2 km altitude are located in the northeastern part of the eyewall,

and at 8 km they are located in the eastern part of the eyewall, resulting in an anticyclonic rotation with height. The magnitude of the temperature anomalies decreases with height.

The wavenumber-1 asymmetries of perturbation pressure  $p'$  also show a consistent picture over time. The pressure perturbations are maximized around a radius of approximately 30 km (Fig. 8d) similar to the temperature perturbations. In contrast to the temperature perturbations, however, the pressure perturbations rotate cyclonically with height. At 2 km, the positive pressure perturbations are located in the northeastern part of the eyewall. At 8 km, the positive pressure perturbations are located in the western part of the eyewall. The pressure perturbations are weakest at midlevels.

Following previous observational (Hence and Houze 2011; DeHart et al. 2014; Foerster et al. 2014) and modeling (Chen and Gopalakrishnan 2015; Rios-Berrios et al. 2016a,b; Leighton et al. 2018) studies, we analyze the data into shear-relative quadrants using the local shear direction of  $114^\circ$ . The quadrants are denoted in Fig. 8d, with south roughly corresponding to "downshear right" where convective-initiation is commonly observed in previous studies. East roughly corresponds to "downshear left", the quadrant with the largest radar reflectivities due to maturing convection. North roughly corresponds to "upshear left", the quadrant containing dissipating cells, and west roughly corresponds to "upshear right", the quadrant with the shallowest convection. The average characteristics within each quadrant and over time are assessed by calculating spatio-temporal averages. First, the dataset for each period was split up into quadrants, then the datasets of all four periods were combined quadrantwise. Vertical cross sections representing the mean structure of each quadrant over time were calculated by averaging the data within each quadrant and over all four periods.

The spatio-temporal averages illustrate the variability of the kinematic and thermodynamic structure from quadrant to quadrant (Figs. 9 and 10). The radar reflectivity exhibits a pattern of convective initiation, maturation and dissipation. In addition, our dataset allows analysis of the

shear-related wavenumber-1 dynamic and thermodynamic forcing terms (Eq. 1) in each quadrant. For easier interpretation, the negative vertical gradient of perturbation pressure is displayed in Figs. 9 and 10 instead of perturbation pressure itself. Positive values of either  $\theta'_\rho$  or  $-dp'/dz$  result in an upward forcing. Note that the thermodynamic fields are not shown below 2 km, because the assumption of gradient-wind balance is not valid in the boundary layer, therefore the perturbation fields are not well-defined. We note that strong mechanical lifting in the boundary layer also plays a critical role in forcing vertical motion, but we are unable to analyze boundary layer forcing with the current analysis technique.

The downshear right quadrant (Figs. 9a-c) exhibits the smallest radar reflectivity values of all four quadrants. The RMW, only discernible at low levels, is located outside of 30 km. The wavenumber-1 perturbation pressure gradient shows positive forcing at upper levels, collocated with the outflow layer, and negative forcing at lower levels. A region of upward motion at upper levels is evident around a radius of 30 km near the upward pressure gradient forcing region. The vertical motion is close to zero throughout most of the domain, believed to be due to averaging of the relatively weaker up- and downdrafts in this quadrant (c.f. Figs. 2 and 3). The wavenumber-1 perturbation temperature shows warm values at low levels and cold values in the outflow layer, resulting in decreased static stability in this quadrant.

Cyclonically downstream, the radar signature in the downshear left quadrant (Figs. 9d-f) suggests the presence of maturing deep convection. The 20-dBZ surface reaches up to almost 10 km and the reflectivity values at midlevels are larger than at the ground, which indicates that the convection is still in its initial stage. This quadrant has low-level inflow and upper level outflow in active eyewall convection, with a broad area of strong ascent, accompanied by air cascading down the inner edge of the eyewall. The low-level inflow is relatively deep, reaching up to about 3.5 km and penetrating inward to about 20 km radius. The wavenumber-1 pressure gradient is positive up to about 9 km.

It is maximized at low levels around a radius 30 km. The wavenumber-1 perturbation temperature shows negative values in a broad area below 9 km, maximized at around 4 km altitude in the region of largest radar reflectivities.

The upshear left quadrant (Figs. 10a-c) contains the largest radar reflectivities exceeding 35 dBZ just outside of 30 km radius. We note that the large reflectivity values at low-levels observed in this quadrant are due in part to the hydrometeor production in the downshear left quadrant that has been advected downstream (Feng and Bell 2019). The RMW slopes outward with height, reaching from about 26 km radius at 1 km altitude out to about 32 km at 12 km altitude. The isotachs at the inner edge of the eyewall exhibit the largest slope of all quadrants, whereas the isotachs fall off slowly outside the RMW. The wavenumber-1 perturbation pressure gradient and thermodynamic fields are oppositely signed to those in the downshear right quadrant, suggesting a transition region where the thermodynamic forcing is becoming less favorable for deep convection. The column of upward vertical motion is weaker, less broad, and more upright than in the previous quadrant. It is flanked by strong downward motion at the inner edge of the eyewall and outside 35 km at upper levels. The perturbation pressure gradient is upward below about 5 km, collocated with low-level outflow, and downward at upper levels, collocated with weak inflow. This temperature pattern with cold anomalies at low levels and warm anomalies at upper levels results in a positive vertical potential temperature gradient, increasing the static stability in this quadrant.

The upshear right quadrant (Figs. 10e-f) contains strong radar reflectivities, but the convection is not as intense or as wide-spread as in the previous quadrant. The tallest reflectivity signature is located inside of 30 km radius. The RMW is pronounced, and located radially outside of the reflectivity maximum. The outflow is quite deep at low levels, stretching up to 6 km altitude at its maximum extent. At upper levels, the outflow is confined to inner radii, meeting deep inflow at around 30 km radius. The wavenumber-1 perturbation pressure gradient has negative values

throughout most of the domain. It is maximized at low levels around a radius 30 km. The eyewall region between 20 and 30 km radius exhibits negative vertical velocities throughout the depth of the column, with the strongest downward motion at midlevels around 6 to 8 km altitude. The downward motion is accompanied by positive wavenumber-1 temperature perturbations below the level of maximum descent.

Azimuth-height composites of the wavenumber-1 components (Fig. 11) combine the findings of all four quadrants and highlight how the fields rotate differently with height. Data of the eyewall region ( $20 \text{ km} \leq r \leq 40 \text{ km}$ ) of all four periods were used to create these composites. The azimuthal distribution of radar reflectivity shows the largest radar reflectivities in the left-of-shear quadrants, and an anticyclonic rotation with height. The isentropes  $\bar{\theta}_\rho + \theta'_{\rho 1}$  ( $\theta'_{\rho 1}$  denotes the wavenumber-1 component of  $\theta_\rho$ ) illustrate the adiabatic lifting in the downshear quadrants and the adiabatic subsidence in the upshear quadrants. The isentropes are consistent with the vertical velocity pattern that shows maximum ascent in the downshear-left quadrant and maximum descent in the upshear-right quadrant. Similar to the radar reflectivity pattern, the azimuthal distribution of temperature perturbations shows an anti-cyclonic rotation with height. In contrast, the pressure perturbations show a cyclonic rotation with height similar to the vorticity pattern. The vertical velocity is the only variable that shows an upright wavenumber-1 pattern. Tangential and radial velocities show patterns with opposite orientation for levels below and above 6 km altitude. The regions of largest tangential velocities are collocated with the regions of largest radar reflectivities.

Overall, the shear-relative spatio-temporal averages of Hurricane Rita on 23 September show a storm structure that is similar to that of other sheared storms indicating convective initiation, maturation, and dissipation around the asymmetric eyewall (Black et al. 2002; Reasor and Eastin 2012; DeHart et al. 2014; Foerster et al. 2014; Feng and Bell 2019). The three-dimensional thermodynamic retrieval provided here for the first time yields new insights into the asymmetric

convective forcing mechanisms on the vortex scale. Deep inflow at low levels and strong upward motion in the downshear-left quadrant is accompanied by a deep upward perturbation pressure gradient and negative temperature perturbations. Downward motion and strong outflow at low levels in the upshear-right quadrant is accompanied by a downward perturbation pressure gradient and positive temperature perturbations. The downshear-right and upshear-left quadrants are transition zones between the strongest forcing in the other two quadrants, with initiating and maturing convection, respectively.

#### *b. Higher-order Wavenumbers: Eyewall Convection*

VWS primarily affects the wavenumber-1 patterns, whereas higher wavenumbers are associated with eyewall mesovortices and the eyewall convection itself (Braun et al. 2006). High-resolution airborne radar data can provide a very detailed look at the structure of the eyewall, but with the RAINEX flight patterns the radar data can not resolve the evolution of individual convective cells since the data has to be composited over about 30 minutes. The cyclonic advection of the eyewall convection with the mean tangential wind acts to blur the results, complicating the interpretation of the higher-order wavenumbers in terms of individual convective cells. To provide insight, a statistical approach is taken to examine the thermodynamic properties of higher-order updrafts in the eyewall. Specifically, the relationship of thermodynamic properties with upward motion and upward acceleration is examined in this manuscript.

A histogram of the perturbation density potential temperature  $\theta'_\rho$  of all updrafts in the eyewall region ( $15 \text{ km} \leq r \leq 40 \text{ km}$ ,  $2 \text{ km} \leq z \leq 12 \text{ km}$ ) for the four different periods (Fig. 12a) shows that the distributions are similar for all periods and are shifted toward negative values. These distributions include all gridpoints with positive vertical velocities, ranging from values just above zero to strong updrafts. The average perturbation density potential temperature computed from these histograms

ranges between -0.48 K and -0.70 K for the four different periods. This shift to negative values is largely due to the fact that most updrafts occur in the downshear quadrants, and that these downshear quadrants exhibit a shear-induced wavenumber-1 cold anomaly. The shear-induced wavenumber-1, however, is quasi-balanced. It makes sense to look at the perturbation density potential temperature not only relative to a vortex in thermal wind balance, but additionally include the shear-induced wavenumber-1 into the reference state. The distributions of this "unbalanced" perturbation density potential temperature (Fig. 12b) show a Gaussian shape centered around zero for all periods, with the majority of the gridpoints exhibiting temperature perturbations of less than 2 K (e-folding is approximately  $\pm 2$  K). Hence, there are approximately the same number of positively buoyant and negatively buoyant updrafts with respect to a reference state which includes shear effects. Limiting the distributions to gridpoints with vertical velocities in excess of  $5 \text{ m s}^{-1}$  results in a shift of the distribution to the right (Fig. 12c). Gridpoints with strong vertical motion are more likely to have positive than negative temperature perturbations.

To test the robustness of this result, average temperature perturbations for gridpoints exceeding a certain vertical velocity threshold are computed. Thresholds are chosen as increments of  $1 \text{ m s}^{-1}$ , from 0 to  $10 \text{ m s}^{-1}$ . Only gridpoints in the downshear quadrants are included to focus on the earlier times of the convective lifecycle.

All periods show monotonically increasing average temperature perturbations with increasing vertical velocity (Fig. 13a). The last values for 2140 UTC and 2210 UTC are an exception and are most likely due to the limited number of gridpoints exceeding the respective threshold. The increase is strongest for 2040 UTC, but all periods show a dependence of the average temperature perturbation on the velocity threshold, with higher temperature perturbations for stronger updrafts.

In contrast, no dependence of the average vertical velocity can be found with increasing temperature perturbation thresholds (Fig. 13b). Similar to thresholding on the vertical velocity, as

in Fig. 13a, for this calculation we thresholded on the unbalanced density potential temperature perturbations in increments of 0.33 K, from 0 to 3 K, and then averaged the vertical velocities of these gridpoints. All periods show a positive, constant average vertical velocity up to a threshold of 2 K. Above that, the average vertical velocity decreases for all periods, except 2140 UTC. Hence, on average, gridpoints with strong updrafts have higher, positive temperature perturbations, but gridpoints with higher temperature perturbations do not necessarily have stronger updrafts. There is no direct correlation between temperature perturbations and vertical velocity. Higher vertical velocities are accompanied by stronger positive temperature anomalies, but the magnitude of the temperature anomalies does not indicate the strength of the vertical velocity.

The occurrence of positive temperature anomalies and upward vertical velocities do not have to be collocated to be linked though. Air parcels with negligible vertical velocities might encounter regions with enhanced temperature anomalies at lower levels, be accelerated upwards by them, and then show increased vertical velocities later on. Results from trajectory analysis of high-resolution simulations (e.g. Braun 2002; Cram et al. 2007; Hazelton et al. 2017) and observational studies (Eastin et al. 2005b; Barnes and Fuentes 2010; Dolling and Barnes 2012; Guimond et al. 2016) suggest that one forcing mechanism for convective bursts in the eyewall is buoyancy through exchange of air between the eye and eyewall.

To analyze the importance of buoyancy for eyewall convection, we investigate the correlation between vertical acceleration and its two forcing terms, buoyancy and vertical perturbation pressure gradient force:

$$\frac{1}{c_p \bar{\theta}_\rho} \frac{Dw}{Dt} = -\frac{\partial \pi'}{\partial z} + \frac{g}{c_p \bar{\theta}_\rho^2} \theta'_\rho \quad (7)$$

expressed in terms of normalized perturbation pressure  $\pi'$ , density potential temperature perturbation  $\theta'_\rho$ , and mean density potential temperature  $\bar{\theta}_\rho$ . This equation is part of the retrieval formulation of SAMURAI-TR and thus has been used to obtain the temperature and pressure fields

that are now being evaluated. However, as noted in FB17 and discussed below, the impact of the vertical momentum equation on the retrieved fields is small and thus it is valid to use the vertical momentum equation as a diagnostic tool. Due to the 30-minute time interval between analyses, the time tendency is neglected in the material derivative of the vertical wind, denoted here as  $C = \frac{Dw}{Dt}$ . The correlation between the vertical acceleration ( $C$ ) and the dynamic ( $C_1 = -\frac{\partial \pi'}{\partial z}$ ) and buoyant ( $C_2 = \frac{g}{c_p \theta_p^2} \theta'_p$ ) forcing, respectively, is expressed in terms of coefficients of determination (hereafter  $R^2$  values). The  $R^2$  values indicate the percentage of variance explained by the dependent variables. Vertical acceleration, dynamic forcing, and buoyant forcing were first computed and then decomposed into wavenumbers. The  $R^2$  values for different wavenumbers in each individual period are summarized in Table 2, and scatter plots for all four periods combined are shown in Fig. 14.

The scatter plots for wavenumber 0-and-1 show that while both forcing terms have non-zero values, the vertical acceleration is very close to zero. This is reflected in  $R^2$  values which are very close or equal to zero, and supports the interpretation of a ‘quasi-balanced’ wavenumber-1 pattern, with negligible vertical acceleration and a near-cancellation between buoyant and dynamic forcings. While gradient wind balance has been previously shown in observations to be a good approximation for the axisymmetric vortex above the boundary layer (Willoughby 1990), we are unaware of quantitative observational support that shows that the wavenumber-1 vertical motion is indeed quasi-balanced with respect to the wavenumber-1 buoyant and dynamic forcing terms. We use the term ‘quasi-balanced’ here to indicate that  $\frac{Dw}{Dt}$  is small on this scale regardless of the strength of the buoyant and dynamic forcings, suggesting that the hydrostatic approximation is valid but that gradient wind balance is more difficult to assess for asymmetric flow (see Brill (2014) for discussion on how the gradient wind depends on the definition of the parcel trajectory and its curvature). Whether the observed wavenumber-1 structure conforms to other theoretical

balance relationships (Raymond 1992; Shapiro and Montgomery 1993) is beyond the scope of the current study and reserved for future work.

At wavenumber 2-and-higher scales, however, correlations between vertical acceleration and the forcing terms are evident. The spread is somewhat large, but the correlation between vertical acceleration and buoyancy is positive, whereas the correlation between vertical acceleration and vertical perturbation pressure gradient force is negative. We believe that the spread is likely due to a combination of uncertainty in  $w$  and the thermodynamic retrieval, the effects of low-pass filtering, and neglect of the time-tendency in the  $\frac{Dw}{Dt}$  calculation. Despite these uncertainties, the thermodynamic forcing terms can explain much of the variance in the observed vertical velocity, with  $R^2$  values as high as 0.26 for the dynamic forcing term at 2140 UTC, and as high as 0.58 for the buoyant forcing term at 2110 UTC (Table 2). The sensitivity of these results to the inclusion of the vertical momentum equation in the retrieval formulation was tested by performing thermodynamic retrievals without the vertical momentum equation for each of the four periods. The mean  $R^2$  values for wavenumber 2-and-higher changed only slightly in response, with a reduction of the mean  $R^2$  value by 0.05 for the dynamic forcing term and by 0.01 for the thermodynamic forcing term. The sensitivity test confirms that the observed results are physical and not a result of a prescribed relationship in the retrieval itself. The  $R^2$  values for wavenumber 2-and-higher indicate that vertical accelerations in convection are correlated with the higher-order wavenumber thermodynamic structure. The positive correlation of vertical acceleration to the buoyant forcing term and higher explanation of variance suggests that buoyancy has a more direct impact on eyewall convection than the dynamic forcing above the boundary layer. The negative correlation of vertical acceleration to the dynamic forcing term and lower explanation of variance suggests that thermodynamic and dynamic forcing may partially counteract each other (Smith et al. 2005).

## 5. Summary and Conclusions

Investigating the physical mechanisms that force and shape eyewall convection is essential to better understand the impacts of the eyewall convection on the storm scale and to estimate how changes in environmental forcing will alter the eyewall convection. Kinematic and thermodynamic observations within the eyewall are critical to identify these physical mechanisms. However, high resolution observations in this region are limited. They are limited temporally to periods when reconnaissance or research aircraft sample the storm, and limited spatially to aircraft tracks, dropsonde paths and scanning geometries of remote sensing instruments. Here, we apply the recently developed thermodynamic retrieval method SAMURAI-TR to observations in Hurricane Rita collected on 23 September 2005 during the RAINEX field campaign. The retrieval provides estimates of the pressure and temperature fields within the inner core region of TCs using airborne Doppler radar data. The retrieved pressure and temperature fields along with the wind and precipitation structure of Hurricane Rita emphasize the impact of vertical wind shear on the azimuthal location of convection in the eyewall. The pressure and temperature fields show the dynamic and thermodynamic processes that act to balance the vortex tilt. Analysis of the contributions of the retrieved pressure and temperature fields to different azimuthal wavenumbers suggests the interpretation of eyewall convection within a three-level framework of balanced, quasi-balanced, and unbalanced motions.

At the time of observation on 23 September 2005, Rita had weakened to a Category-3 hurricane due to its exposure to increased VWS, cooler sea surface temperatures, and structural changes that had occurred on the previous day. Four consecutive 30-min intervals of data paint a very consistent picture of the main kinematic and thermodynamic features of the eyewall. During all four periods, the vortex tilt is to the northeast, approximately perpendicular to the storm motion. The vortex

tilts downshear relative to the large-scale shear, and left-of-shear relative to the local shear. Most previous studies found that the tilt had an orientation close to the left-of-shear direction. Hence, the local shear seems to be more representative than the SHIPS large-scale shear in this case. Vertical motion and precipitation structure show a pronounced wavenumber-1 pattern in all cases, with largest radar reflectivities toward the north and strongest upward motion toward the north and east.

The 2-D axisymmetric tangential wind fields from the center out to 60 km radius are balanced by a pressure deficit of approximately 26 hPa and a temperature increase of approximately 4 K. The pressure deficit is maximized at low levels, while the temperature increase is maximized at vertical levels of 6 to 9 km. This axisymmetric mean temperature and pressure fields represent the vortex reference state in thermal wind balance.

The pressure and temperature fields obtained by SAMURAI-TR show pronounced wavenumber-1 patterns. The patterns are very consistent over all four periods, bolstering the confidence in the retrieval and suggesting a connection between the thermodynamic structure of the vortex and the environmental wind shear. The results of the thermodynamic retrieval and interaction of the vortex with shear are summarized schematically in Fig. 15. The temperature perturbations show an anticyclonic rotation with height, with negative values in the northern part (upshear left) of the eyewall at low levels and negative values in the eastern part (downshear left) of the eyewall at upper levels. Hence, the cold anomalies are located in theowntilt direction and are collocated with regions of strong convection. Jones (1995) identified this thermal couplet with cool anomaliesowntilt and warm anomalies uptilt as the adiabatic response of the vortex to shear. The shear introduces a tilt of the vortex and the tilt introduces adiabatic ascent right-of-tilt and adiabatic descent left-of-tilt, resulting in raised isentropes and thus cold anomaliesowntilt and lowered isentropes and thus warm anomalies uptilt. This wavenumber-1 in vertical motion and temperature acts to balance the tilt and thus keep the vortex close to alignment and in a quasi-steady state.

Hence, the combination of balanced-state and wavenumber-1 will be called the quasi-balanced reference state in our three-level framework. The anticyclonic rotation of the thermal anomalies with height is similar to results of Jones (2000). She also found an anticyclonic rotation with height in her simulations of baroclinic vortices and attributed it to the anticyclonic rotation of the tilt with height, emphasizing the close connection between the orientation of the thermal couplet and the tilt direction. The wavenumber-1 pressure perturbations in Rita show a cyclonic rotation with height, with high pressure anomalies to the north of the center at low levels and high pressure anomalies to the west of the center at upper levels. Hence, the high pressure anomalies are located predominantly left-of-shear, with low-level storm-relative inflow and upper-level storm-relative outflow to the east of the center, and a reverse flow pattern to the west of the center. The pressure perturbation distribution results in an upward-directed pressure gradient force at upper levels in the downshear-right quadrant, at all vertical levels in the downshear-left quadrant, and at low levels in the upshear-left quadrant. In contrast, it results in a downward-directed pressure gradient force at upper levels in the upshear-left quadrant, at all vertical levels in the upshear-right quadrant, and at low levels in the downshear-right quadrant.

Individual convective cells embedded in the eyewall have been regarded to play an integral role in eyewall dynamics ("hot towers", Malkus and Riehl (1960); Hendricks et al. (2004)) and their location has been linked to intensity change efficiency (Pendergrass and Willoughby 2009; Vigh and Schubert 2009). Individual convective cells project onto higher-order wavenumbers. The temporal resolution of 30 minutes between our radar analyses precludes a detailed analysis of the thermodynamic structure of individual updrafts. Nevertheless, statistical analysis of the higher-wavenumber structure of convective updrafts suggests that while "stronger updrafts are more likely to be buoyant" the opposite conclusion that "more buoyant parcels have higher vertical velocities" is not supported by our data. These findings are consistent with the results of Eastin

et al. (2005a). Their statistical analysis of aircraft data of 14 intense hurricanes similarly showed that while stronger updrafts are more likely to be buoyant the more buoyant parcels do not always have higher vertical velocities. This highlights the difference between vertical motion and vertical acceleration, and the necessity to analyze the effects of buoyancy on an air parcel along a parcel trajectory rather than instantaneously.

Correlations between vertical acceleration and dynamic and thermodynamic forcing, respectively, suggest that vertical accelerations are due to higher-order wavenumbers and that the thermodynamic forcing dominates the dynamic forcing. Wavenumbers-0 and -1 of the vertical acceleration show very small acceleration values and no correlation to the forcing terms, indicating that these lower wavenumbers are near hydrostatic balance or "quasi-balanced", suggesting that the forcing of the individual convective elements should be studied with respect to a quasi-balanced reference state. Higher wavenumbers of vertical acceleration show non-zero values and a correlation to both forcing terms, where the correlation to the thermodynamic forcing is stronger and positive and the correlation to the dynamic forcing term is weaker and negative. The results indicate that the vertical acceleration of individual convective air parcels in the eyewall above the boundary layer is linked to thermal forcing, and that buoyancy and perturbation pressure gradients tend to counteract each other.

In summary, the radar-derived kinematic and thermodynamic structure of Hurricane Rita on 23 September 2005 enabled a very detailed analysis of the thermodynamic and dynamic forcing of eyewall convection. The structure can be best described in terms of a three-level framework of balanced, quasi-balanced, and unbalanced motions. The axisymmetric (wavenumber-0) structure is determined by a primary force *balance* between the gravitational force and the vertical pressure gradient force in the vertical, and the horizontal pressure gradient force, Coriolis force, and centrifugal force in the horizontal, resulting in a pressure drop and temperature increase toward

the center. The wavenumber-1 structure, is determined by the interaction of the storm with environmental VWS, resulting in a *quasi-balance* between shear and shear-induced kinematic and thermodynamic anomalies. The vortex (represented by a vorticity column) gets tilted, producing wavenumber-1 pressure anomalies, which are balanced by a wavenumber-1 pattern in vertical motion and temperature, represented by sloping isentropes (Fig. 15). The wavenumber-1 vertical motion is still largely hydrostatic. The higher-order wavenumbers are connected to *unbalanced* motions and convective cells within the eyewall, with the higher-order vertical acceleration being linked to thermal forcing.

Future work applying the retrieval to other datasets and analyzing the thermodynamic structure of tropical cyclones at different stages of their lifecycle or while being impacted by different environmental conditions will help to improve the understanding of the physical mechanisms that determine the activity and organization of eyewall convection. Analysis of the respective importance of the thermodynamic and dynamic forcing terms during those different scenarios should lead to a better understanding of how eyewall convection contributes to tropical cyclone intensity change.

*Acknowledgments.* AMB gratefully acknowledges the valuable comments and suggestions of committee members Gary Barnes, Jennifer Griswold, Patrick Harr, Albert Kim, Wen-Chau Lee and her advisor (MMB) during the preparation of her Ph.D. dissertation at the University of Hawai‘i at Mānoa (a portion of which the present study reports). We thank the three anonymous reviewers for their helpful and insightful comments. We acknowledge the RAINEX field campaign for collecting the data used in this manuscript. We thank John Beven (National Hurricane Center) for providing us with the SHIPS data. The research was supported by the National Science Foundation

under Awards AGS-1349881 and AGS-1701225 and the Office of Naval Research under Award N000141410118.

*Data availability statement.* The data underlying the findings within this article can be accessed upon request.

## References

- Bargen, D. W., and R. C. Brown, 1980: Interactive radar velocity unfolding. *Preprints, 19th Radar Meteor. Conf., 9-13 Sept. 1997*, Amer. Meteor. Soc.
- Barnes, G. M., and P. Fuentes, 2010: Eye Excess Energy and the Rapid Intensification of Hurricane Lili (2002). *Mon. Wea. Rev.*, **138**, 1446–1458.
- Bell, M. M., W.-C. Lee, C. A. Wolff, and H. Cai, 2013: A Solo-Based Automated Quality Control Algorithm for Airborne Tail Doppler Radar Data. *J. Appl. Meteor. Climatol.*, **52**, 2509–2528.
- Bell, M. M., M. T. Montgomery, and K. A. Emanuel, 2012a: Air-Sea Enthalpy and Momentum Exchange at Major Hurricane Wind Speeds Observed during CBLAST. *J. Atmos. Sci.*, **69**, 3197–3222.
- Bell, M. M., M. T. Montgomery, and W. C. Lee, 2012b: An Axisymmetric View of Concentric Eyewall Evolution in Hurricane Rita (2005). *J. Atmos. Sci.*, **69**, 2414–2432.
- Beven, J. L., and Coauthors, 2008: Atlantic hurricane season of 2005. *Monthly Weather Review*, **136** (3), 1109 – 1173, doi:10.1175/2007MWR2074.1, URL <https://journals.ametsoc.org/view/journals/mwre/136/3/2007mwr2074.1.xml>.

Black, M. L., J. F. Gamache, F. D. Marks, C. E. Samsury, and H. E. Willoughby, 2002: Eastern Pacific Hurricanes Jimena of 1991 and Olivia of 1994: The Effect of Vertical Shear on Structure and Intensity. *Mon. Wea. Rev.*, **130**, 2291–2312.

Bosart, B. L., W.-C. Lee, and R. M. Wakimoto, 2002: Procedures to Improve the Accuracy of Airborne Doppler Radar Data. *J. Atmos. Oceanic Technol.*, **19**, 322–339.

Braun, S. A., 2002: A Cloud-Resolving Simulation of Hurricane Bob (1991): Storm Structure and Eyewall Buoyancy. *Mon. Wea. Rev.*, **130**, 1573–1592.

Braun, S. A., M. T. Montgomery, and Z. Pu, 2006: High-Resolution Simulation of Hurricane Bonnie (1998). Part I: The Organization of Eyewall Vertical Motion. *J. Atmos. Sci.*, **63**, 19–42.

Brill, K. F., 2014: Revisiting an old concept: The gradient wind. *Monthly Weather Review*, **142** (4), 1460 – 1471, doi:10.1175/MWR-D-13-00088.1, URL <https://journals.ametsoc.org/view/journals/mwre/142/4/mwr-d-13-00088.1.xml>.

Cai, H., W.-C. Lee, M. M. Bell, C. A. Wolff, X. Tang, and F. Roux, 2015: A Generalized Navigation Correction Method for Airborne Doppler Radar Data. *Preprints, 37th Conference on Radar Meteorology, 14 - 18 September 2015*, Norman, OK, Amer. Meteor. Soc.

Chen, H., and S. G. Gopalakrishnan, 2015: A Study on the Asymmetric Rapid Intensification of Hurricane Earl (2010) Using the HWRF System. *J. Atmos. Sci.*, **72**, 531–550.

Corbosiero, K. L., and J. Molinari, 2002: The Effects of Vertical Wind Shear on the Distribution of Convection in Tropical Cyclones. *Mon. Wea. Rev.*, **130**, 2110–2123.

Corbosiero, K. L., and J. Molinari, 2003: The Relationship between Storm Motion, Vertical Wind Shear, and Convective Asymmetries in Tropical Cyclones. *Mon. Wea. Rev.*, **60**, 366–376.

Cram, T. A., J. Persing, M. T. Montgomery, and S. A. Braun, 2007: A Lagrangian Trajectory View on Transport and Mixing Processes between the Eye, Eyewall, and Environment Using a High-Resolution Simulation of Hurricane Bonnie (1998). *J. Atmos. Sci.*, **64**, 1835–1856.

DeHart, J., R. A. Houze, Jr., and R. F. Rogers, 2014: Quadrant Distribution of Tropical Cyclone Inner-Core Kinematics in Relation to Environmental Shear. *J. Atmos. Sci.*, **71**, 2713–2732.

DeMaria, M., and J. Kaplan, 1994: A Statistical Hurricane Intensity Prediction Scheme (SHIPS) for the Atlantic Basin. *Wea. Forecasting*, **9**, 209–220.

DeMaria, M., C. R. Sampson, J. A. Knaff, and K. D. Musgrave, 2014: Is Tropical Cyclone Intensity Guidance Improving? *Bull. Amer. Meteor. Soc.*, **95**, 387–398, doi:10.1175/BAMS-D-12-00240.1.

Didlake, A. C., Jr., and R. A. Houze, Jr., 2011: Kinematics of the Secondary Eyewall Observed in Hurricane Rita (2005). *J. Atmos. Sci.*, **68**, 1620–1636.

Didlake, A. C., Jr., and R. A. Houze, Jr., 2013a: Convective-Scale Variations in the Inner-Core Rainbands of a Tropical Cyclone. *J. Atmos. Sci.*, **70**, 504–523.

Didlake, A. C., Jr., and R. A. Houze, Jr., 2013b: Dynamics of the Stratiform Sector of a Tropical Cyclone Rainband. *J. Atmos. Sci.*, **70**, 1891–1911.

Dolling, K. P., and G. M. Barnes, 2012: The Creation of a High Equivalent Potential Temperature Reservoir in Tropical Storm Humberto (2001) and Its Possible Role in Storm Deepening. *Mon. Wea. Rev.*, **140**, 492–505.

Eastin, M. D., W. M. Gray, and P. G. Black, 2005a: Buoyancy of Convective Vertical Motions in the Inner Core of Intense Hurricanes. Part I: General Statistics. *Mon. Wea. Rev.*, **133**, 188–208.

Eastin, M. D., W. M. Gray, and P. G. Black, 2005b: Buoyancy of Convective Vertical Motions in the Inner Core of Intense Hurricanes. Part II: Case Studies. *Mon. Wea. Rev.*, **133**, 209–227.

Emanuel, K. A., 1995: Sensitivity of tropical cyclones to surface exchange coefficients and a revised steady-state model incorporating eye dynamics. *J. Atmos. Sci.*, **52**, 3969–3976.

Feng, Y.-C., and M. M. Bell, 2019: Microphysical Characteristics of an Asymmetric Eyewall in Major Hurricane Harvey (2017). *Geophysical Research Letters*, **46** (1), 461–471, doi:<https://doi.org/10.1029/2018GL080770>, URL <https://agupubs.onlinelibrary.wiley.com/doi/abs/10.1029/2018GL080770>, <https://agupubs.onlinelibrary.wiley.com/doi/pdf/10.1029/2018GL080770>.

Fischer, M. S., R. F. Rogers, and P. D. Reasor, 2020: The Rapid Intensification and Eyewall Replacement Cycles of Hurricane Irma (2017). *Monthly Weather Review*, **148** (3), 981 – 1004, doi:[10.1175/MWR-D-19-0185.1](https://doi.org/10.1175/MWR-D-19-0185.1), URL <https://journals.ametsoc.org/view/journals/mwre/148/3/mwr-d-19-0185.1.xml>.

Foerster, A. M., 2016: Radar-derived Thermodynamic Structure of a Major Hurricane in Vertical Wind Shear. Ph.D. thesis, University of Hawai‘i at Mānoa, URL <http://hdl.handle.net/10125/51598>.

Foerster, A. M., and M. M. Bell, 2017: Thermodynamic Retrieval in Rapidly Rotating Vortices from Multiple-Doppler Radar Data. *J. Atmos. Oceanic Technol.*, **34**, 2353–2374.

Foerster, A. M., M. M. Bell, P. A. Harr, and S. C. Jones, 2014: Observations of the Eyewall Structure of Typhoon Sinlaku (2008) during the Transformation Stage of Extratropical Transition. *Mon. Wea. Rev.*, **142**, 3372–3392.

Frank, W. M., and E. A. Ritchie, 1999: Effects of environmental flow upon tropical cyclone structure. *Mon. Wea. Rev.*, **127**, 2044–2061.

Gal-Chen, T., 1978: A Method for the Initialization of the Anelastic Equations: Implications for Matching Models with Observations. *Mon. Wea. Rev.*, **106**, 587–606.

Georgis, J. F., F. Roux, and P. H. Hildebrand, 2000: Observation of Precipitating Systems over Complex Orography with Meteorological Doppler Radars: A Feasibility Study. *Meteorol. Atmos. Phys.*, **72**, 185–202.

Guimond, S. R., G. M. Heymsfield, P. D. Reasor, and A. C. Didlake, Jr., 2016: The Rapid Intensification of Hurricane Karl (2010): New Remote Sensing Observations of Convective Bursts from the Global Hawk Platform. *J. Atmos. Sci.*, **73**, 3617–3639.

Guimond, S. R., G. M. Heymsfield, and F. J. Turk, 2010: Multiscale Observations of Hurricane Dennis (2005): The Effects of Hot Towers on Rapid Intensification. *J. Atmos. Sci.*, **67** (3), 633 – 654, doi:10.1175/2009JAS3119.1, URL <https://journals.ametsoc.org/view/journals/atsc/67/3/2009jas3119.1.xml>.

Guimond, S. R., J. A. Zhang, J. W. Sapp, and S. J. Frasier, 2018: Coherent Turbulence in the Boundary Layer of Hurricane Rita (2005) during an Eyewall Replacement Cycle. *J. Atmos. Sci.*, **75** (9), 3071 – 3093, doi:10.1175/JAS-D-17-0347.1, URL <https://journals.ametsoc.org/view/journals/atsc/75/9/jas-d-17-0347.1.xml>.

Hazelton, A. T., R. F. Rogers, and R. E. Hart, 2017: Analyzing Simulated Convective Bursts in Two Atlantic Hurricanes. Part I: Burst Formation and Development. *Mon. Wea. Rev.*, **145**, 3073–3094.

Hence, D. A., and R. A. Houze, Jr., 2011: Vertical structure of hurricane eyewalls as seen by TRMM precipitation radar. *J. Atmos. Sci.*, **68**, 1637–1652.

Hendricks, E. A., M. T. Montgomery, and C. A. Davis, 2004: The Role of "Vortical" Hot Towers in the Formation of Tropical Cyclone Diana (1984). *J. Atmos. Sci.*, **61**, 1209–1232.

Hildebrand, P. H., and Coauthors, 1996: The ELDORA/ASTRAIA Airborne Doppler Weather Radar: High-Resolution Observations from TOGA COARE. *Bull. Amer. Meteor. Soc.*, **77**, 213–232.

Houze, R. A., Jr., and Coauthors, 2006: The Hurricane Rainband and Intensity Change Experiment: Observations and Modeling of Hurricanes Katrina, Ophelia, and Rita. *Bull. Amer. Meteor. Soc.*, **87**, 1503–1521.

Jones, S. C., 1995: The evolution of vortices in vertical shear. I: Initially barotropic vortices. *Q. J. R. Meteorol. Soc.*, **121**, 821–851.

Jones, S. C., 2000: The evolution of vortices in vertical shear. III: Baroclinic vortices. *Q. J. R. Meteorol. Soc.*, **126**, 3161–3186.

Jorgensen, D. P., T. Mateka, and J. D. DuGranrut, 1996: Multi- beam techniques for deriving wind fields from airborne Doppler radars. *Meteor. Atmos. Phys.*, **59**, 83–104.

Knabb, R. D., D. P. Brown, and J. R. Rhome, 2011: Tropical Cyclone Report, Hurricane Rita, 18-26 September 2005. *National Hurricane Center*.

Leighton, H., S. Golalakrishnan, J. A. Zhang, R. F. Rogers, Z. Zhang, and V. Tallapragada, 2018: Azimuthal Distribution of Deep Convection, Environmental Factors, and Tropical Cyclone Rapid Intensification: A Perspective from HWRF Ensemble Forecasts of Hurricane Edouard (2014). *J. Atmos. Sci.*, **75**, 275–295.

Liou, Y.-C., 2001: The Derivation of Absolute Potential Temperature Perturbations and Pressure Gradients from Wind Measurements in Three-Dimensional Space. *J. Atmos. Oceanic Technol.*, **18**, 577–590.

Malkus, J., and H. Riehl, 1960: On the dynamics and energy transformations in steady-state hurricanes. *Tellus*, **12**, 1–20.

Marks, F. D., Jr., R. A. Houze, Jr., and J. F. Gamache, 1992: Dual-Aircraft Investigation of the Inner Core of Hurricane Norbert. Part I: Kinematic Structure. *J. Atmos. Sci.*, **49**, 919–942.

Martinez, J., M. M. Bell, J. L. Vigh, and R. F. Rogers, 2017: Examining Tropical Cyclone Structure and Intensification with the FLIGHT+ Dataset from 1999 to 2012. *Monthly Weather Review*, **145** (11), 4401–4421, doi:10.1175/MWR-D-17-0011.1.

Pendergrass, A. G., and H. E. Willoughby, 2009: Diabatically Induced Secondary Flows in Tropical Cyclones. Part I: Quasi-Steady Forcing. *Mon. Wea. Rev.*, **137**, 805–821, doi:{http://dx.doi.org/10.1175/2008MWR2657.1}.

Raymond, D. J., 1992: Nonlinear Balance and Potential-Vorticity Thinking At Large Rossby Number. *Quart. J. Roy. Meteor. Soc.*, **118** (507), 987–1015, doi:<https://doi.org/10.1002/qj.49711850708>, URL <https://rmets.onlinelibrary.wiley.com/doi/abs/10.1002/qj.49711850708>, <https://rmets.onlinelibrary.wiley.com/doi/pdf/10.1002/qj.49711850708>.

Reasor, P. D., and M. D. Eastin, 2012: Rapidly Intensifying Hurricane Guillermo (1997). Part II: Resilience in Shear. *Mon. Wea. Rev.*, **140**, 425–444.

Reasor, P. D., M. T. Montgomery, and L. D. Grasso, 2004: A New Look at the Problem of Tropical Cyclones in Vertical Shear Flow: Vortex Resiliency. *J. Atmos. Sci.*, **61**, 3–22.

Reasor, P. D., R. Rogers, and S. Lorsolo, 2013: Environmental Flow Impacts on Tropical Cyclone Structure Diagnosed from Airborne Doppler Radar Composites. *Mon. Wea. Rev.*, **141**, 2970–2991.

Rios-Berrios, R., R. D. Torn, and C. A. Davis, 2016a: An Ensemble Approach to Investigate Tropical Cyclone Intensification in Sheared Environments. Part I: Katia (2011). *J. Atmos. Sci.*, **73**, 71–93.

Rios-Berrios, R., R. D. Torn, and C. A. Davis, 2016b: An Ensemble Approach to Investigate Tropical Cyclone Intensification in Sheared Environments. Part II: Ophelia (2011). *J. Atmos. Sci.*, **73**, 1555–1575.

Rogers, R., P. Reasor, and S. Lorsolo, 2013: Airborne Doppler Observations of the Inner-Core Structural Differences between Intensifying and Steady-State Tropical Cyclones. *Mon. Wea. Rev.*, **141**, 2970–2991.

Rogers, R. F., P. D. Reasor, J. A. Zawislak, and L. T. Nguyen, 2020: Precipitation Processes and Vortex Alignment during the Intensification of a Weak Tropical Cyclone in Moderate Vertical Shear. *Monthly Weather Review*, **148** (5), 1899 – 1929, doi:10.1175/MWR-D-19-0315.1, URL <https://journals.ametsoc.org/view/journals/mwre/148/5/mwr-d-19-0315.1.xml>.

Rogers, R. F., P. D. Reasor, and J. A. Zhang, 2015: Multiscale Structure and Evolution of Hurricane Earl (2010) during Rapid Intensification. *Mon. Wea. Rev.*, **143** (2), 536 – 562, doi:10.1175/MWR-D-14-00175.1, URL <https://journals.ametsoc.org/view/journals/mwre/143/2/mwr-d-14-00175.1.xml>.

Roux, F., 1985: Retrieval of Thermodynamic Fields from Multiple-Doppler Radar Data Using the Equations of Motion and the Thermodynamic Equation. *Mon. Wea. Rev.*, **113**, 2142–2157.

Shapiro, L. J., and M. T. Montgomery, 1993: A Three-Dimensional Balance Theory for Rapidly Rotating Vortices. *J. Atmos. Sci.*, **50**, 3322 – 3335, doi:10.1175/1520-0469(1993)050<3322:ATDBTF>2.0.CO;2.

Smith, R. K., 2006: Accurate determination of a balanced axisymmetric vortex in a compressible atmosphere. *Tellus A*, **58**, 98–103.

Smith, R. K., M. T. Montgomery, and H. Zhu, 2005: Buoyancy in tropical cyclones and other rapidly rotating atmospheric vortices. *Dyn. Atmos. Oceans*, **40**, 189–208.

Testud, J., P. H. Hildebrand, and W.-C. Lee, 1995: A Procedure to Correct Airborne Doppler Radar Data for Navigation Errors Using the Echo Returned from the Earth's Surface. *J. Atmos. Oceanic Technol.*, **12**, 800–820.

Trabing, B. C., and M. M. Bell, 2020: Understanding Error Distributions of Hurricane Intensity Forecasts during Rapid Intensity Changes. *Wea. Forecasting*, **35**, 2219–2234, doi:10.1175/WAF-D-19-0253.1.

Vigh, J. L., and W. H. Schubert, 2009: Rapid Development of the Tropical Cyclone Warm Core. *J. Atmos. Sci.*, **66**, 3335–3350.

Viltard, N., and F. Roux, 1998: Structure and Evolution of Hurricane Claudette on 7 September 1991 from Airborne Doppler Radar Observations. Part II: Thermodynamics. *Mon. Wea. Rev.*, **126**, 281–302.

Wang, Y., and G. J. Holland, 1996: Tropical cyclone motion and evolution in vertical shear. *J. Atmos. Sci.*, **53**, 3313–3352.

Willoughby, H. E., 1990: Gradient Balance in Tropical Cyclones. *J. Atmos. Sci.*, **47**, 265–274.

Willoughby, H. E., 2009: Diabatically Induced Secondary Flows in Tropical Cyclones. Part II: Periodic Forcing. *Mon. Wea. Rev.*, **137**, 822–835.

Zhang, D.-L., Y. Liu, and M. K. Yau, 2000: A Multiscale Numerical Study of Hurricane Andrew (1992). Part III: Dynamically Induced Vertical Motion. *Mon. Wea. Rev.*, **128**, 3772–3788.

## LIST OF TABLES

TABLE 1. Statistics of the center position of Hurricane Rita and its vertical tilt derived from SAMURAI analyses on 23 September 2005. Center positions for the four periods are in degrees latitude and longitude. The tilt is calculated between 8 km and 2 km altitude, and the tilt direction is defined using the meteorological convention.

time	center lat (°)	center lon (°)	tilt magnitude (km)	tilt direction (°)
2040 UTC	-92.56	28.23	5.0	53
2110 UTC	-92.63	28.30	5.0	37
2140 UTC	-92.68	28.38	2.2	63
2210 UTC	-92.74	28.45	4.2	45

TABLE 2.  $R^2$  values characterizing the relation between vertical acceleration and thermodynamic/dynamic forcing in the vertical momentum equation for each of the four periods and their combination. The  $R^2$  values are computed separately for wavenumbers 0-and-1 (Wnrs 0&1), and wavenumbers-2 and higher (Wnr  $\geq 2$ ).

	2040 UTC	2110 UTC	2140 UTC	2210 UTC	total
Wnrs 0&1, Dynamic	0.02	0.00	0.00	0.01	0.00
Wnrs 0&1, Thermodynamic	0.00	0.00	0.00	0.01	0.00
Wnr $\geq 2$ , Dynamic	0.15	0.19	0.03	0.26	0.14
Wnr $\geq 2$ , Thermodynamic	0.39	0.58	0.28	0.47	0.42

## LIST OF FIGURES

- Fig. 1.** (top) National Hurricane Center best-track position of Hurricane Rita, with the open hurricane symbol denoting tropical storm strength, the closed symbol denoting hurricane strength, and L denoting a remnant low. (center) Best-track intensity in terms of maximum sustained winds (knots, blue line) and minimum pressure (hPa, green line). The observation period is indicated by the vertical grey bar. (bottom) Flight tracks of NRL P-3 (blue), NOAA 43 (green), and NOAA 42 (red) into Hurricane Rita during the period of interest (2020 UTC to 2230 UTC), overlaid on GOES-12 Band 1 Reflectance at 2125 UTC 23 September 2005. . . . . 48
- Fig. 2.** Horizontal cross sections of SAMURAI radar reflectivity (shaded, dBZ), horizontal velocity (black arrows,  $\text{m s}^{-1}$ ), and vertical velocity (white contours,  $\text{m s}^{-1}$ ) at 2 km, 5 km, and 8 km altitude for (left column) 2040 UTC and (right column) 2110 UTC. Flight tracks are overlaid at 5 km altitude. . . . . 49
- Fig. 3.** Horizontal cross sections of SAMURAI analyses for (left column) 2140 UTC and (right column) 2210 UTC as in Fig. 2. . . . . 50
- Fig. 4.** Schematic of storm center positions, tilt directions, and environmental shear for all four periods. The center positions (black circles) and the tilt directions (small purple arrows) are derived from the respective SAMURAI analyses (see text). The two insets illustrate the SHIPS shear (upper right) and the local shear derived from the SAMURAI analyses (lower left), with the red arrows indicating the deep-layer shear directions and the orange arrows indicating the shallow-layer directions. . . . . 51
- Fig. 5.** (left column) Azimuthally-averaged storm structure of radar reflectivity (shaded, dBZ) and tangential wind speed ( $\text{m s}^{-1}$ ) for (a) 2040 UTC, (b) 2110 UTC, (c) 2140 UTC, and (d) 2210 UTC. (right column) Mean pressure deficit (blue dashed, hPa) and mean temperature increase (red solid, K) relative to the mean pressure and temperature at a radius of 60 km at each respective vertical level for (e) 2040 UTC, (f) 2110 UTC, (g) 2140 UTC, and (h) 2210 UTC. . . . . 52
- Fig. 6.** Horizontal cross sections at 5 km altitude of (left column) perturbation pressure (shaded, hPa) and (right column) perturbation density potential temperature (shaded, K) for 2040 UTC, 2110 UTC, 2140 UTC, and 2210 UTC. Radar reflectivity (black contours at 20, 30, 40, and 50 dBZ) is added for orientation. . . . . 53
- Fig. 7.** Horizontal cross sections of (a) perturbation pressure (shaded, hPa) and (b) perturbation density potential temperature (shaded, K) at 2, 5, and 8- km altitude for 2140 UTC. Radar reflectivity (black contours at 20, 30, 40, and 50 dBZ) is added for orientation. . . . . 54
- Fig. 8.** Horizontal cross sections of the wavenumber-1 components of (a) vertical velocity (shaded,  $\text{m s}^{-1}$ ), (b) vorticity (shaded,  $10^{-5} \text{ s}^{-1}$ ), (c) perturbation density potential temperature (shaded, K), and (d) perturbation pressure (shaded, hPa) for 2 km (left), 5 km (center), and 8 km altitude (right) for 2140 UTC. The black arrow in the left panels illustrates the local shear direction. A definition of the shear-relative quadrants is overlaid in the bottom right panel. Radar reflectivity (black contours at 20, 30, 40, and 50 dBZ) is added for orientation. . . . . 55
- Fig. 9.** Radius-height cross sections of (a,d) radar reflectivity (shaded, dBZ) and tangential wind speed (contours,  $\text{m s}^{-1}$ ), (b,e) the wavenumber-1 components of vertical perturbation pressure gradient (shaded,  $\text{hPa km}^{-1}$ ) and radial wind speed (contours,  $\text{m s}^{-1}$ ) and (c,f) the wavenumber-1 components of density potential temperature perturbation (shaded, K) and vertical wind speed (contours,  $\text{m s}^{-1}$ ) for (left column) the downshear-right and (right column)

**Fig. 12.** Histograms of perturbation density potential temperature for gridpoints in the eyewall ( $15 \text{ km} \leq r \leq 40 \text{ km}$ ,  $2 \text{ km} \leq z \leq 12 \text{ km}$ ) with positive vertical velocity for each period (red: 2040 UTC, green: 2110 UTC, blue: 2140 UTC, orange: 2210 UTC) for (a) the total  $\theta'_\rho$ , (b) the unbalanced  $\theta'_\rho$ , i.e.  $\theta'_\rho$  minus its wavenumber-1 component, and (c) the unbalanced  $\theta'_\rho$  for all gridpoints with a vertical velocity exceeding  $5 \text{ m s}^{-1}$ . The average  $\theta'_\rho$  for each scenario and period is inserted in the respective plot. . . . . 59

**Fig. 14.** Scatter plots of vertical acceleration (C), dynamic forcing (C1), and thermodynamic forcing (C2) for wavenumbers 0-and-1, and wavenumbers 2-and-higher. The scatter plots contain data of the eyewall region ( $15 \text{ km} \leq r \leq 40 \text{ km}$ ,  $2 \text{ km} \leq z \leq 8 \text{ km}$ ) of all four periods. . . . . 61

**Fig. 15.** Summary schematic of the kinematic and thermodynamic structure of Hurricane Rita (2005). The gray cylinder represents the vortex tower of the eyewall, which is tilted by the environmental wind shear (black vector). Green ‘L’ symbols and vectors denote cyclonic low pressure anomalies, and brown ‘H’ symbols denote anticyclonic high pressure anomalies. Thermal anomalies are denoted by blue (cold) and red (warm) circles and shading. Blue arrows show the modified secondary circulation. The thick black contour denotes a representative potential temperature surface, with arrows illustrating the cyclonic vortex flow around the eyewall. In the downshear right quadrant, air parcels move cyclonically downstream and adiabatically upward along the potential temperature surface resulting in individual convective motions denoted by the cumulus cloud and upward arrow. A warm anomaly is shown in the convective cloud to denote the release of latent heat associated with the buoyant updraft. . . . 62

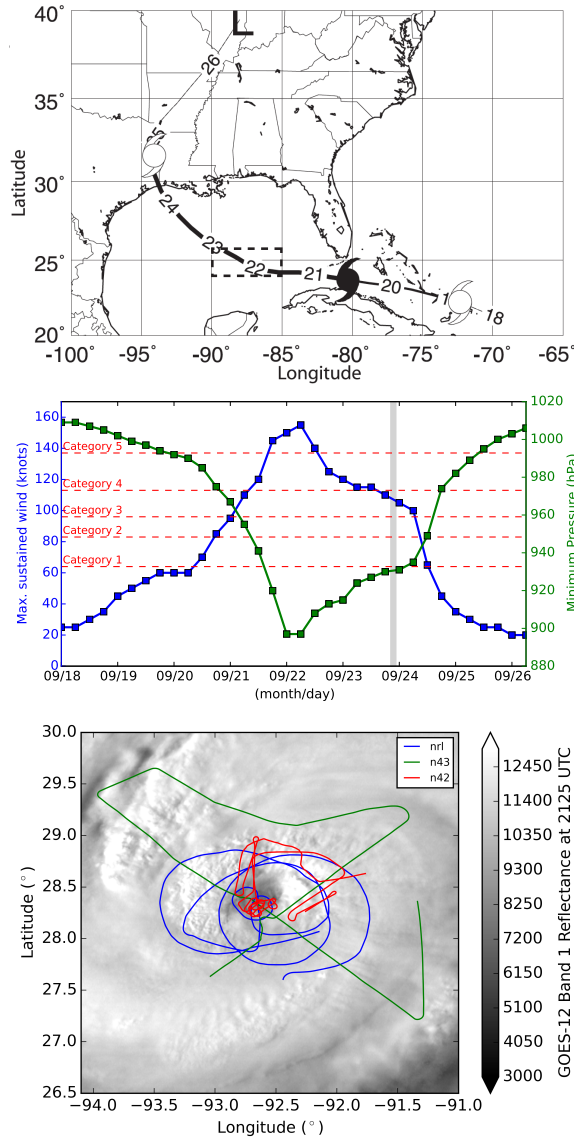


FIG. 1. (top) National Hurricane Center best-track position of Hurricane Rita, with the open hurricane symbol denoting tropical storm strength, the closed symbol denoting hurricane strength, and L denoting a remnant low. (center) Best-track intensity in terms of maximum sustained winds (knots, blue line) and minimum pressure (hPa, green line). The observation period is indicated by the vertical grey bar. (bottom) Flight tracks of NRL P-3 (blue), NOAA 43 (green), and NOAA 42 (red) into Hurricane Rita during the period of interest (2020 UTC to 2230 UTC), overlaid on GOES-12 Band 1 Reflectance at 2125 UTC 23 September 2005.

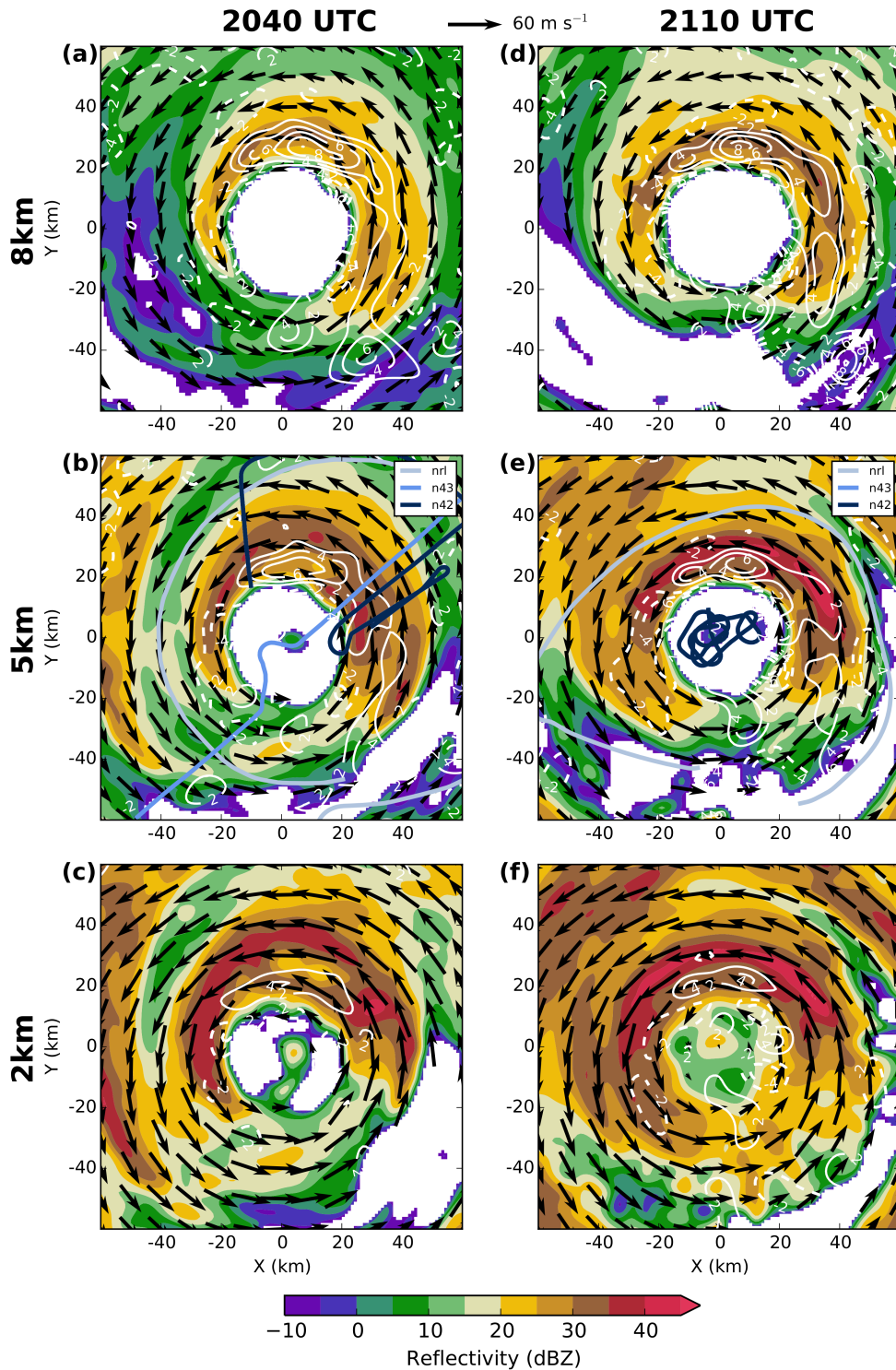


FIG. 2. Horizontal cross sections of SAMURAI radar reflectivity (shaded, dBZ), horizontal velocity (black arrows,  $\text{m s}^{-1}$ ), and vertical velocity (white contours,  $\text{m s}^{-1}$ ) at 2 km, 5 km, and 8 km altitude for (left column) 2040 UTC and (right column) 2110 UTC. Flight tracks are overlaid at 5 km altitude.

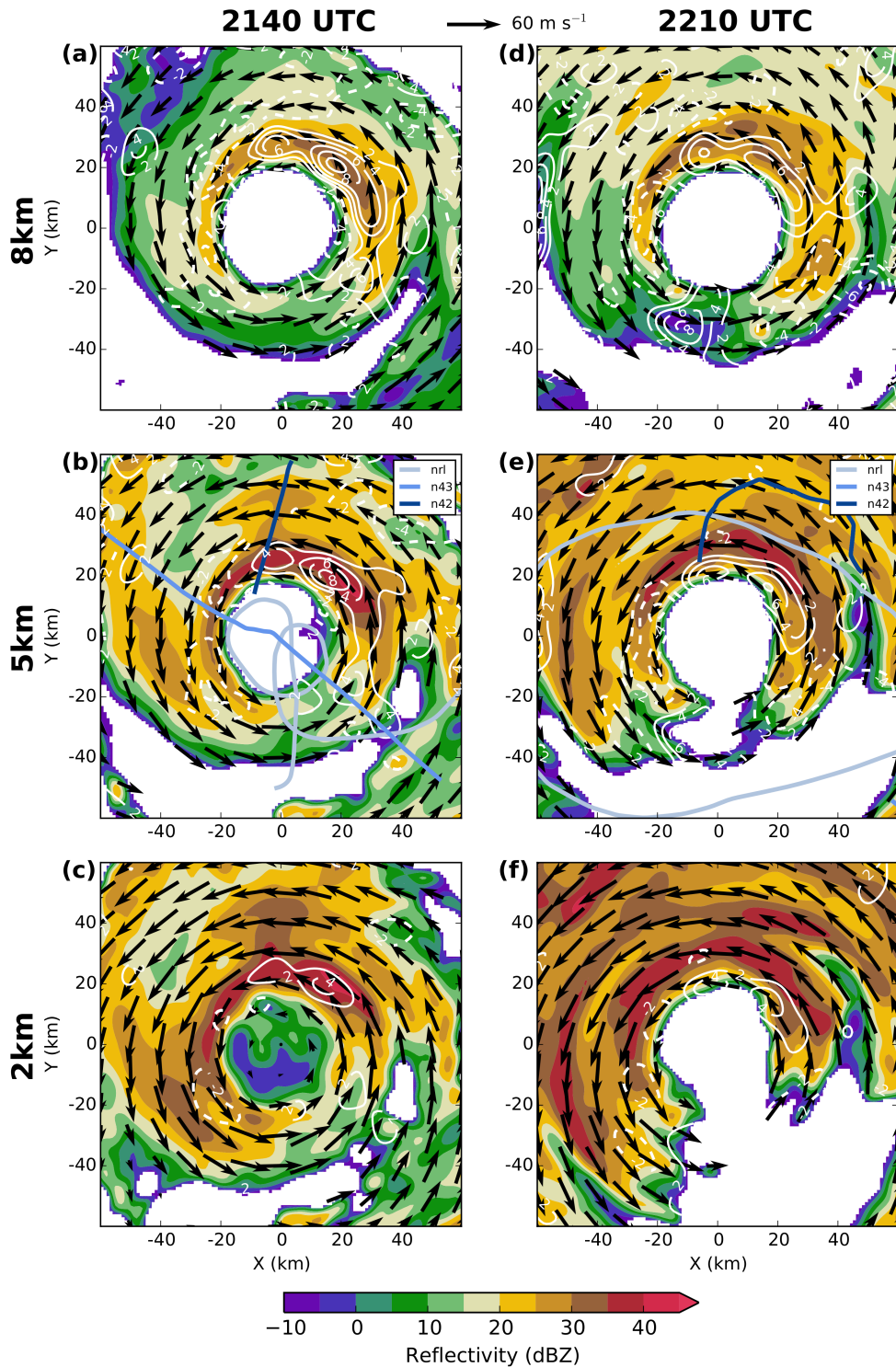


FIG. 3. Horizontal cross sections of SAMURAI analyses for (left column) 2140 UTC and (right column) 2210 UTC as in Fig. 2.

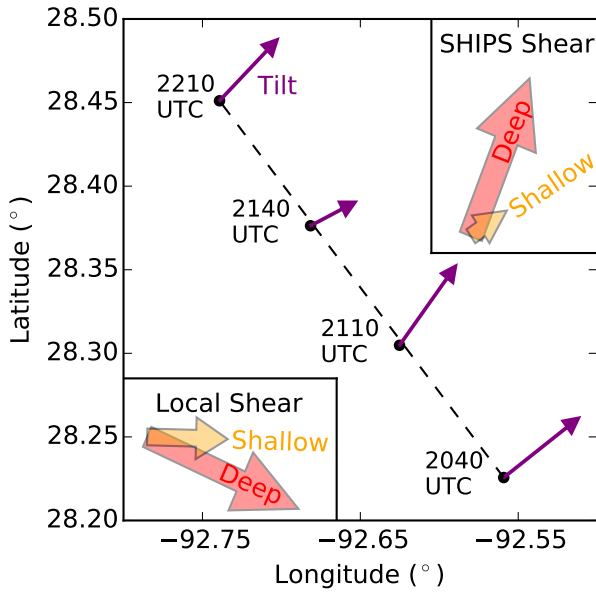


FIG. 4. Schematic of storm center positions, tilt directions, and environmental shear for all four periods. The center positions (black circles) and the tilt directions (small purple arrows) are derived from the respective SAMURAI analyses (see text). The two insets illustrate the SHIPS shear (upper right) and the local shear derived from the SAMURAI analyses (lower left), with the red arrows indicating the deep-layer shear directions and the orange arrows indicating the shallow-layer directions.

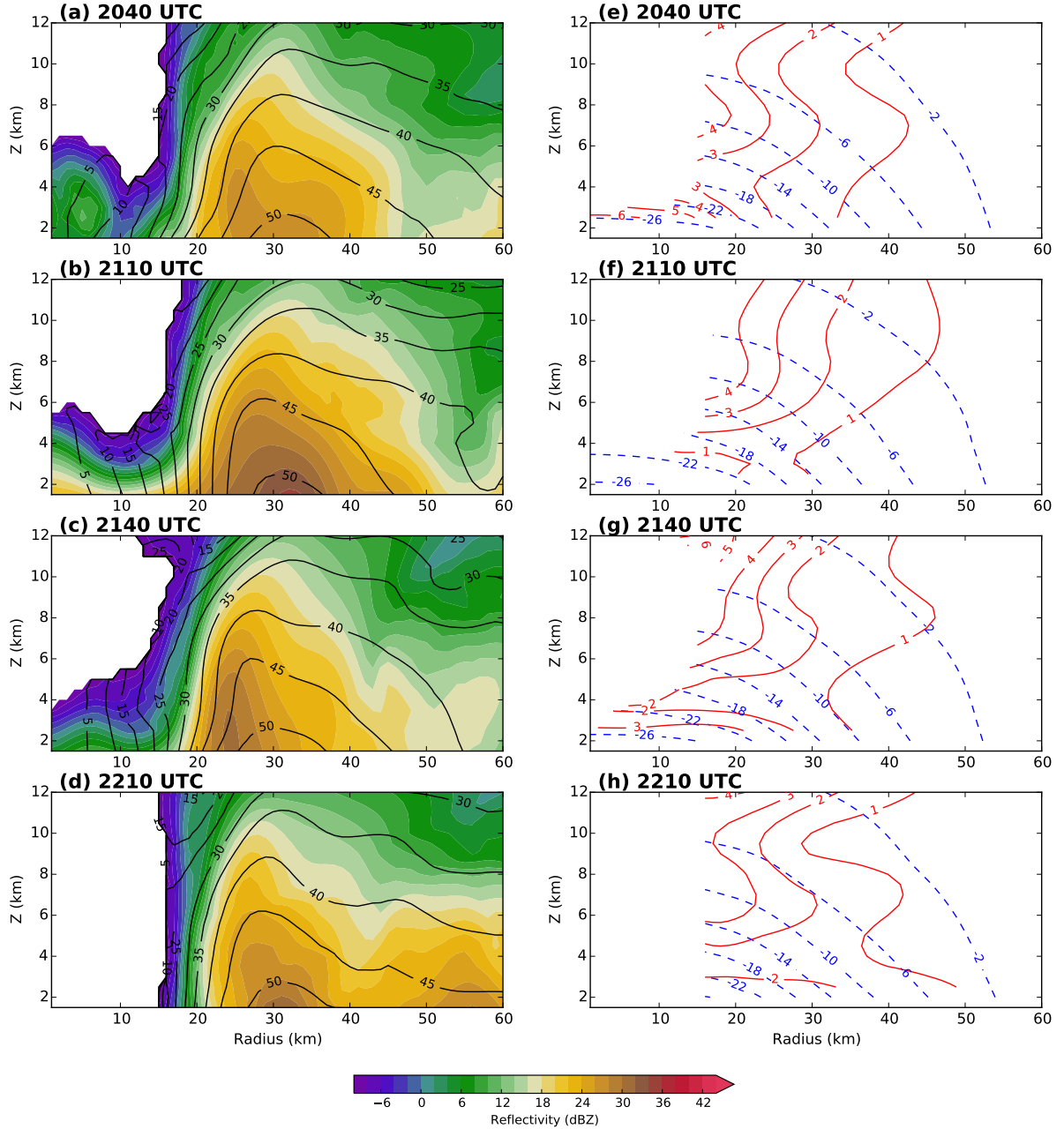


FIG. 5. (left column) Azimuthally-averaged storm structure of radar reflectivity (shaded, dBZ) and tangential wind speed ( $\text{m s}^{-1}$ ) for (a) 2040 UTC, (b) 2110 UTC, (c) 2140 UTC, and (d) 2210 UTC. (right column) Mean pressure deficit (blue dashed, hPa) and mean temperature increase (red solid, K) relative to the mean pressure and temperature at a radius of 60 km at each respective vertical level for (e) 2040 UTC, (f) 2110 UTC, (g) 2140 UTC, and (h) 2210 UTC.

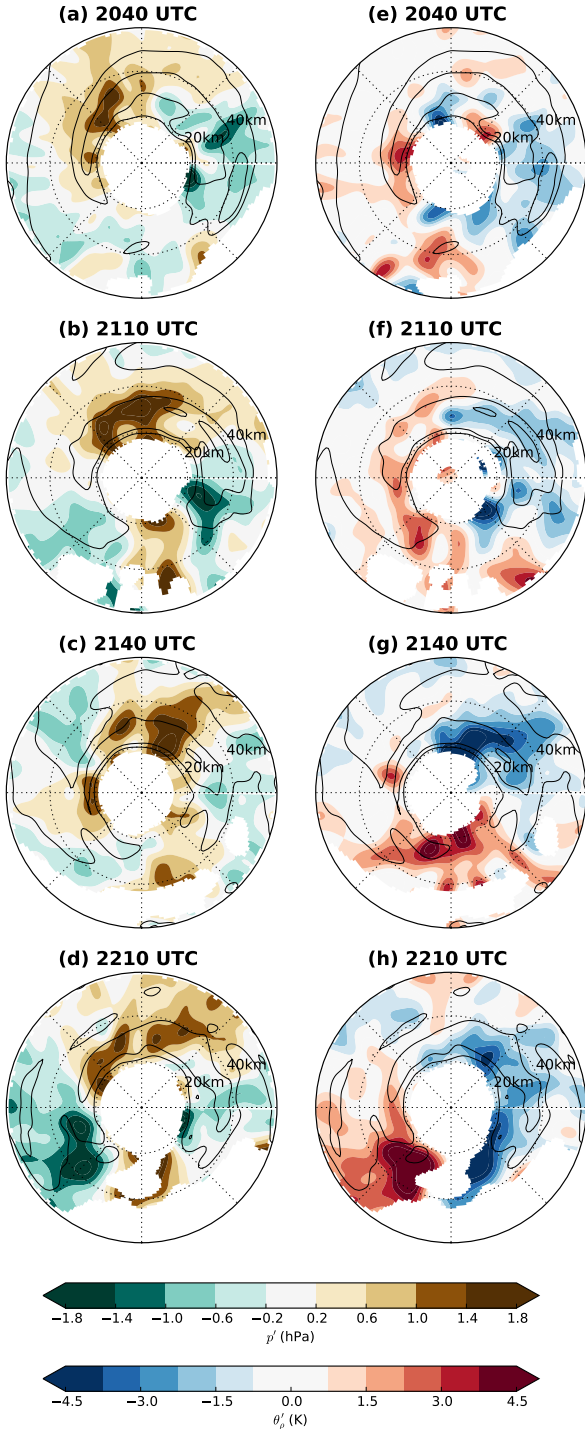


FIG. 6. Horizontal cross sections at 5 km altitude of (left column) perturbation pressure (shaded, hPa) and (right column) perturbation density potential temperature (shaded, K) for 2040 UTC, 2110 UTC, 2140 UTC, and 2210 UTC. Radar reflectivity (black contours at 20, 30, 40, and 50 dBZ) is added for orientation.

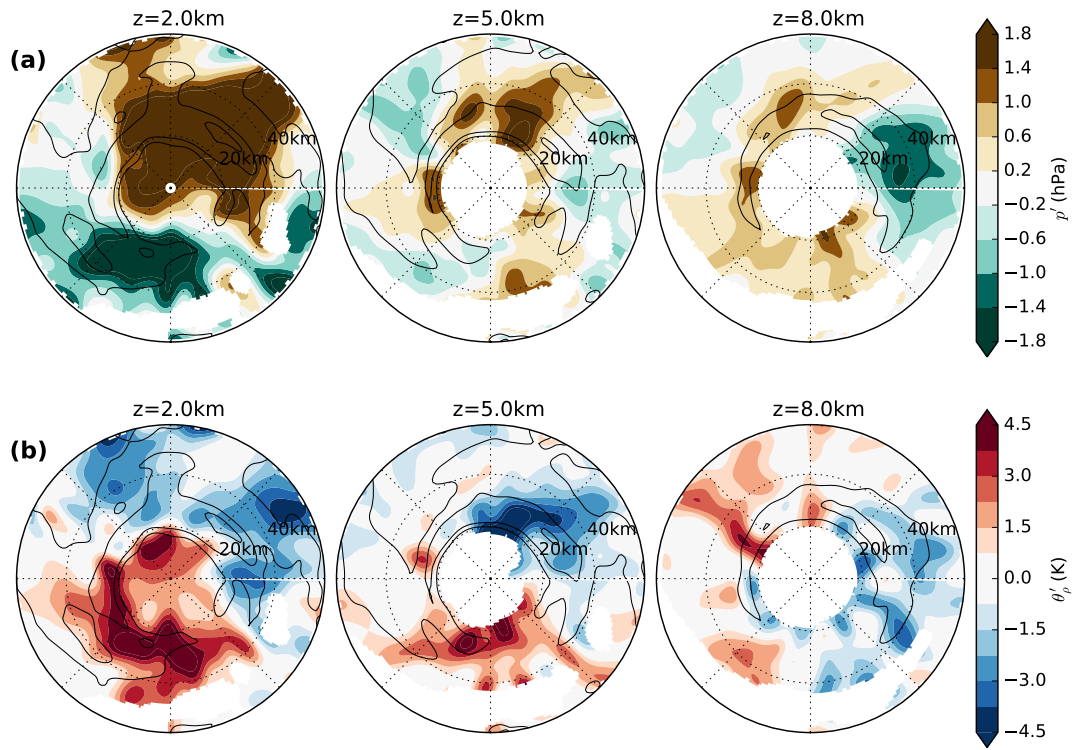


FIG. 7. Horizontal cross sections of (a) perturbation pressure (shaded, hPa) and (b) perturbation density potential temperature (shaded, K) at 2, 5, and 8- km altitude for 2140 UTC. Radar reflectivity (black contours at 20, 30, 40, and 50 dBZ) is added for orientation.

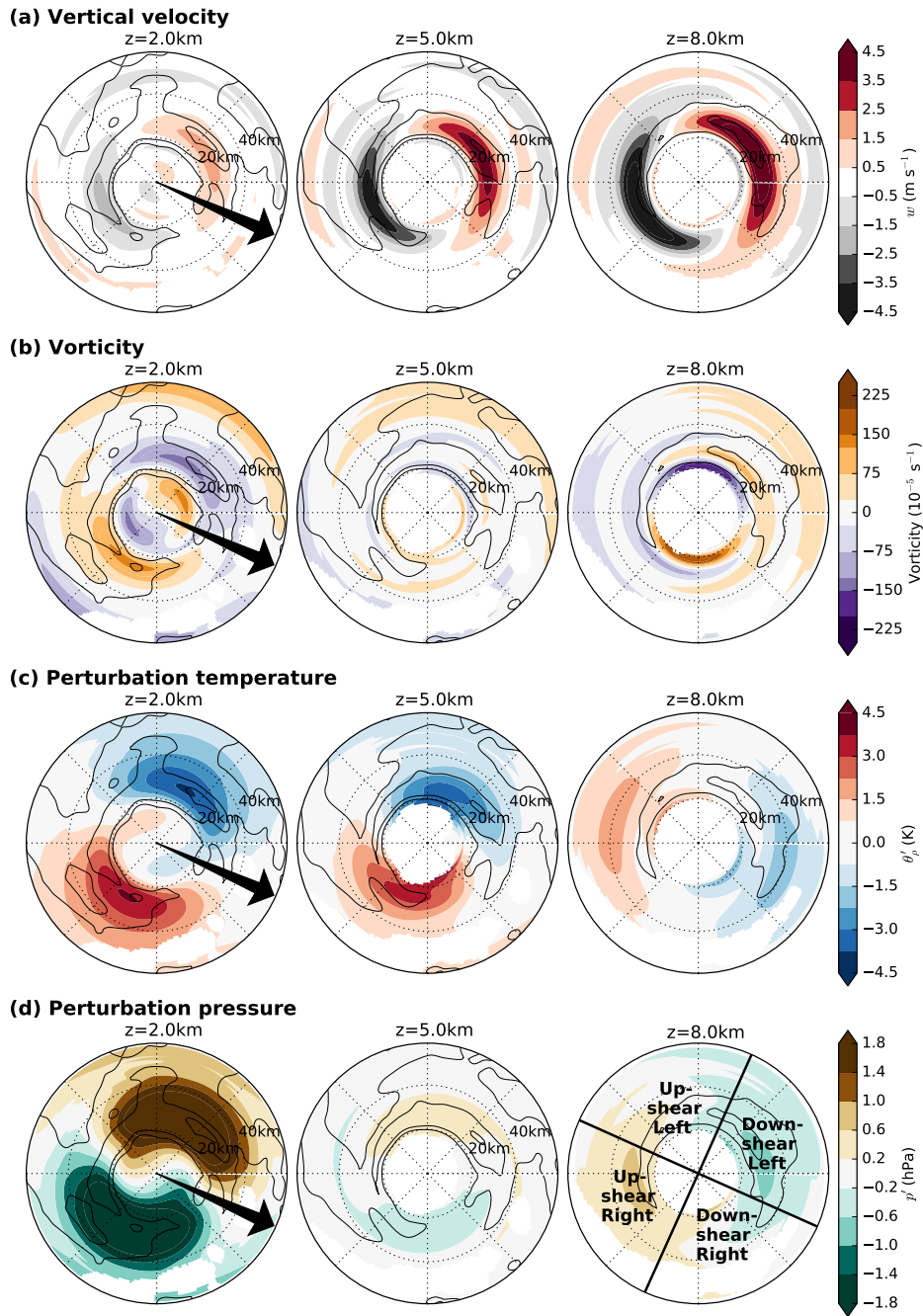


FIG. 8. Horizontal cross sections of the wavenumber-1 components of (a) vertical velocity (shaded,  $\text{m s}^{-1}$ ), (b) vorticity (shaded,  $10^{-5} \text{ s}^{-1}$ ), (c) perturbation density potential temperature (shaded, K), and (d) perturbation pressure (shaded, hPa) for 2 km (left), 5 km (center), and 8 km altitude (right) for 2140 UTC. The black arrow in the left panels illustrates the local shear direction. A definition of the shear-relative quadrants is overlaid in the bottom right panel. Radar reflectivity (black contours at 20, 30, 40, and 50 dBZ) is added for orientation.

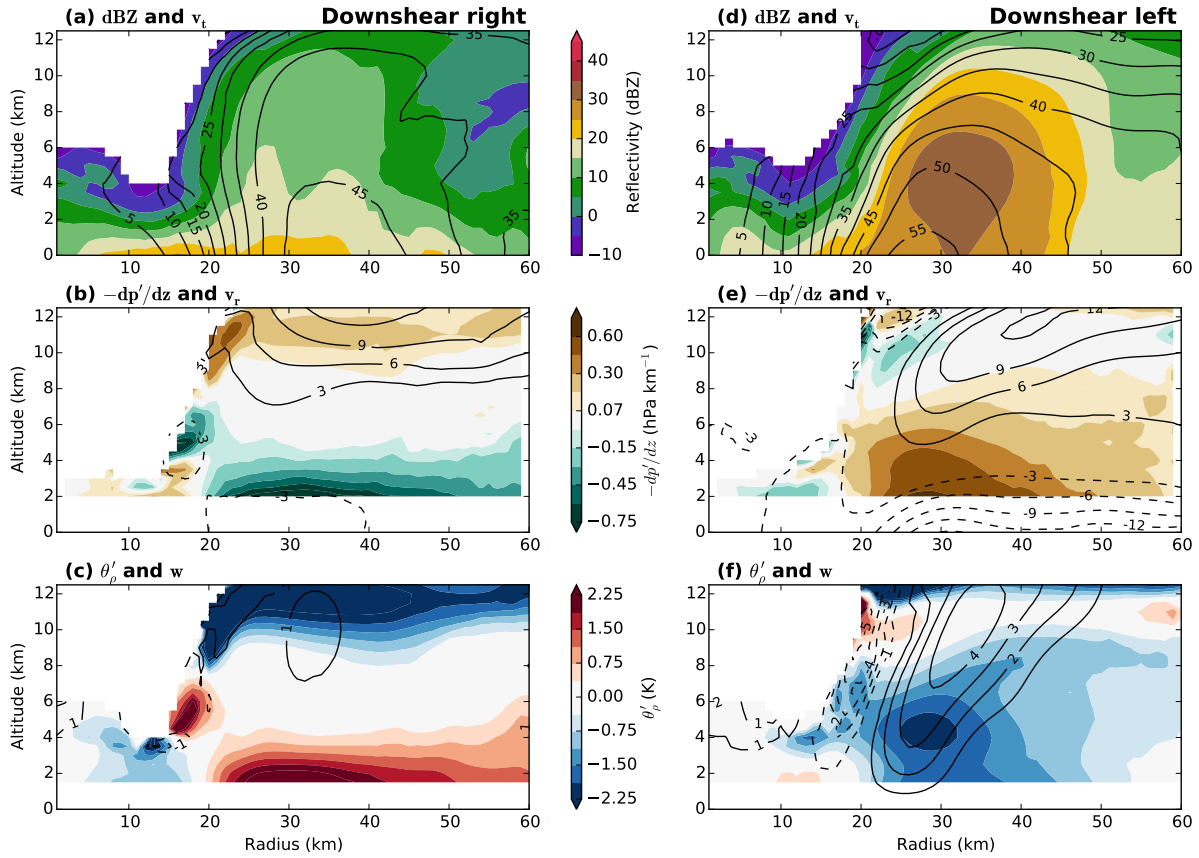


FIG. 9. Radius-height cross sections of (a,d) radar reflectivity (shaded, dBZ) and tangential wind speed (contours,  $m s^{-1}$ ), (b,e) the wavenumber-1 components of vertical perturbation pressure gradient (shaded,  $hPa \text{ km}^{-1}$ ) and radial wind speed (contours,  $m s^{-1}$ ) and (c,f) the wavenumber-1 components of density potential temperature perturbation (shaded, K) and vertical wind speed (contours,  $m s^{-1}$ ) for (left column) the downshear-right and (right column) downshear-left quadrants. The variables are averaged azimuthally within each shear-relative quadrant and over all four periods.

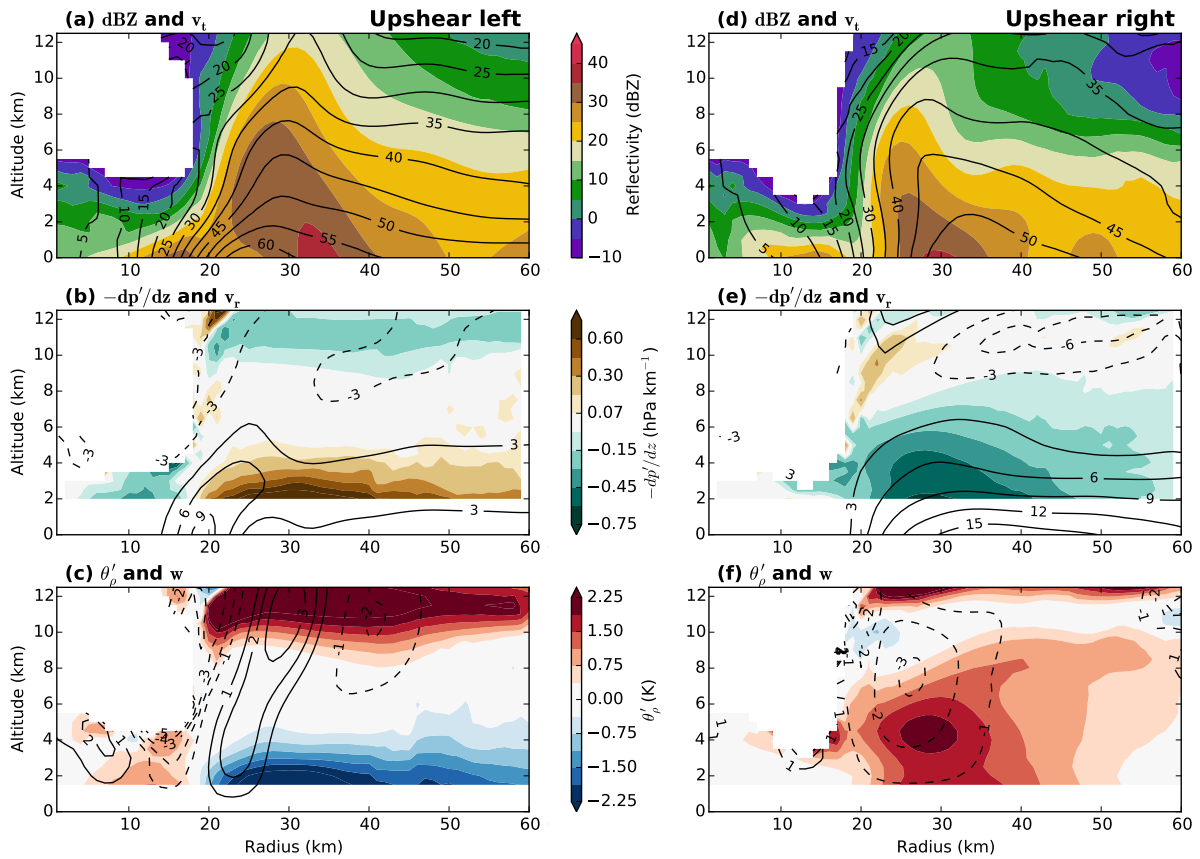


FIG. 10. Same as Fig. 9, but for (left column) the upshear-left and (right column) upshear-right quadrants.

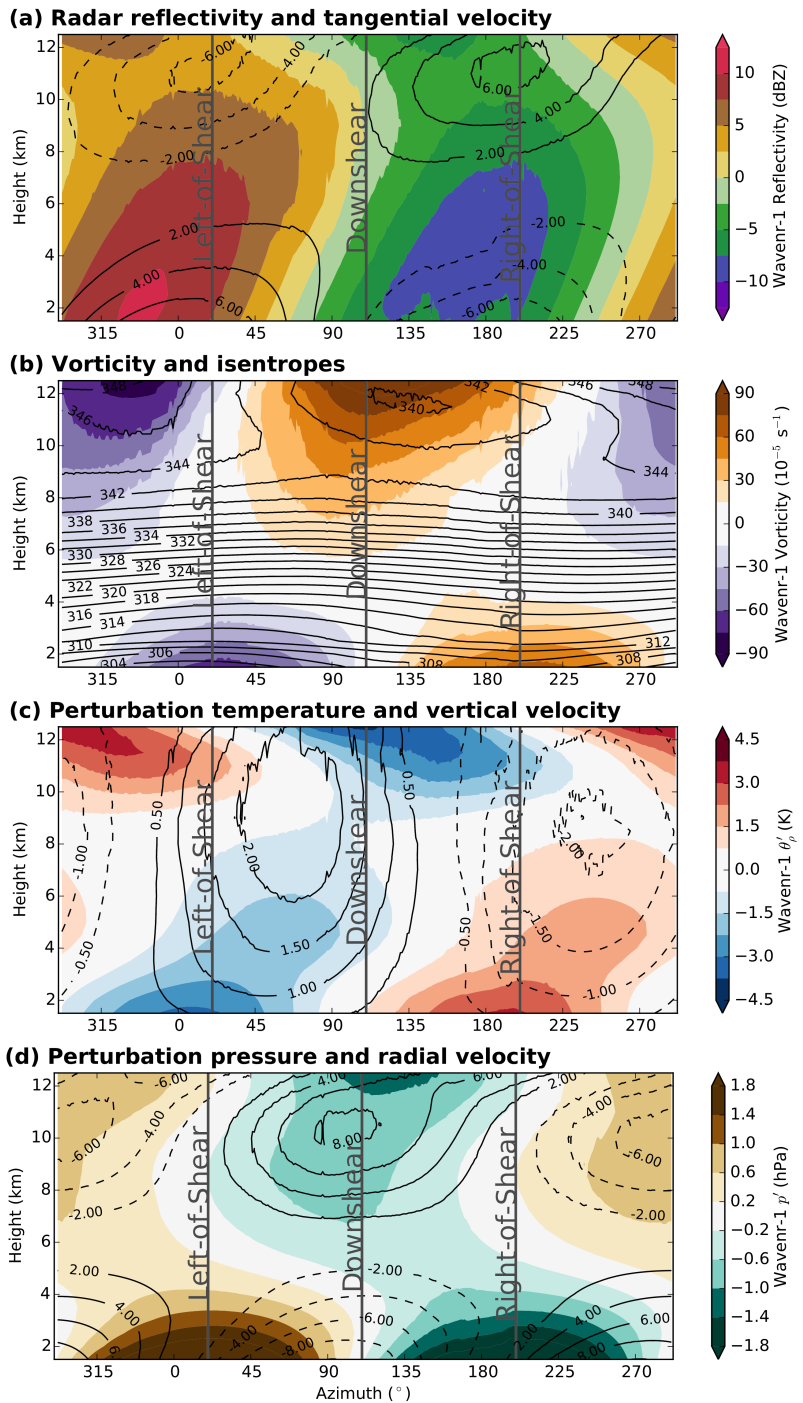


FIG. 11. Azimuth-height composites of the wavenumber-1 components of the eyewall region ( $20 \text{ km} \leq r \leq 40 \text{ km}$ ) of all four periods combined: (a) radar reflectivity (shaded, dBZ) and tangential velocity (contoured,  $\text{m s}^{-1}$ ), (b) vorticity (shaded,  $10^{-5} \text{ s}^{-1}$ ) and isentropes  $\bar{\theta}_\rho + \theta'_{\rho 1}$  (contoured, K), (c) density potential temperature perturbation (shaded, K) and vertical velocity (contoured,  $\text{m s}^{-1}$ ), and (d) perturbation pressure (shaded,  $10^{-3}$ ) and radial velocity (contoured,  $\text{m s}^{-1}$ ).

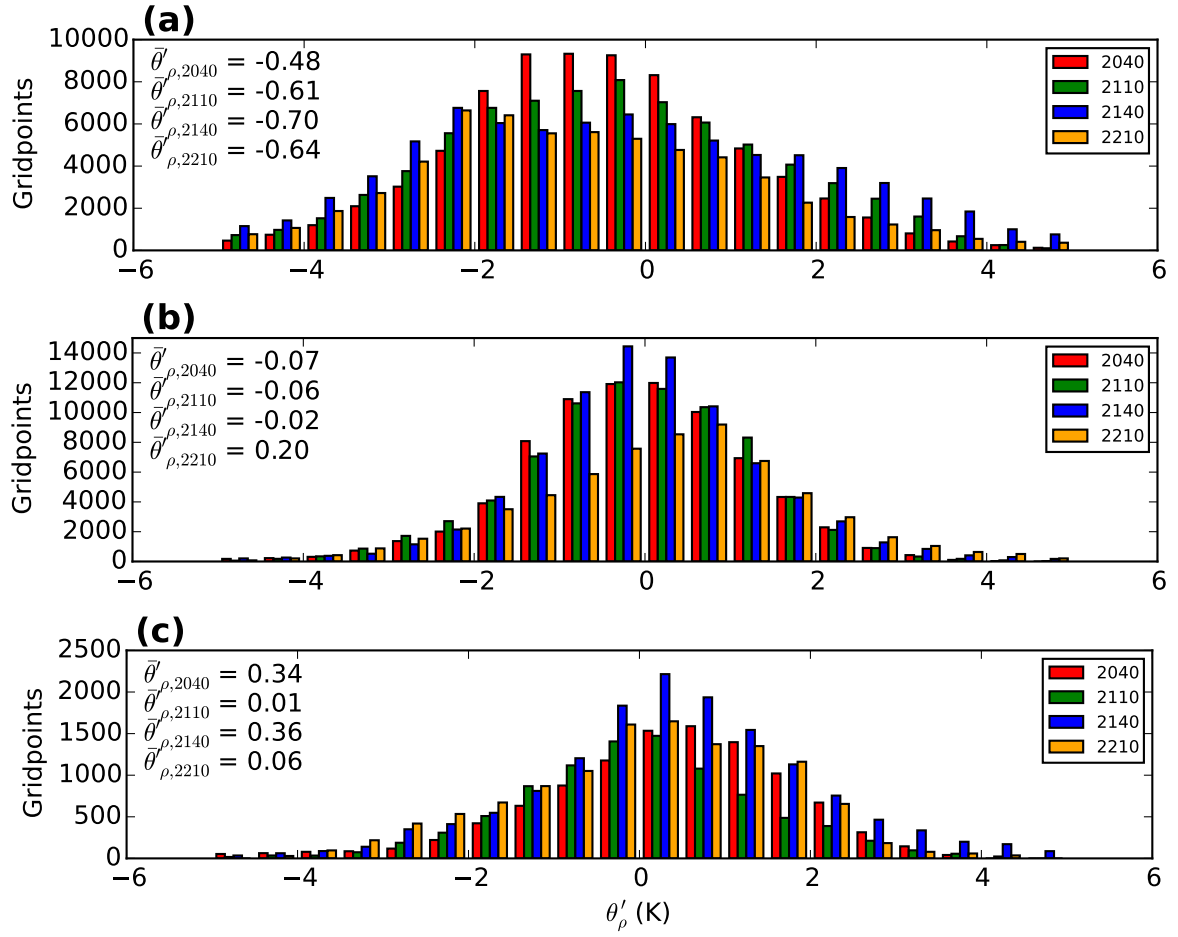


FIG. 12. Histograms of perturbation density potential temperature for gridpoints in the eyewall ( $15 \text{ km} \leq r \leq 40 \text{ km}$ ,  $2 \text{ km} \leq z \leq 12 \text{ km}$ ) with positive vertical velocity for each period (red: 2040 UTC, green: 2110 UTC, blue: 2140 UTC, orange: 2210 UTC) for (a) the total  $\theta'_\rho$ , (b) the unbalanced  $\theta'_\rho$ , i.e.  $\theta'_\rho$  minus its wavenumber-1 component, and (c) the unbalanced  $\theta'_\rho$  for all gridpoints with a vertical velocity exceeding  $5 \text{ m s}^{-1}$ . The average  $\theta'_\rho$  for each scenario and period is inserted in the respective plot.

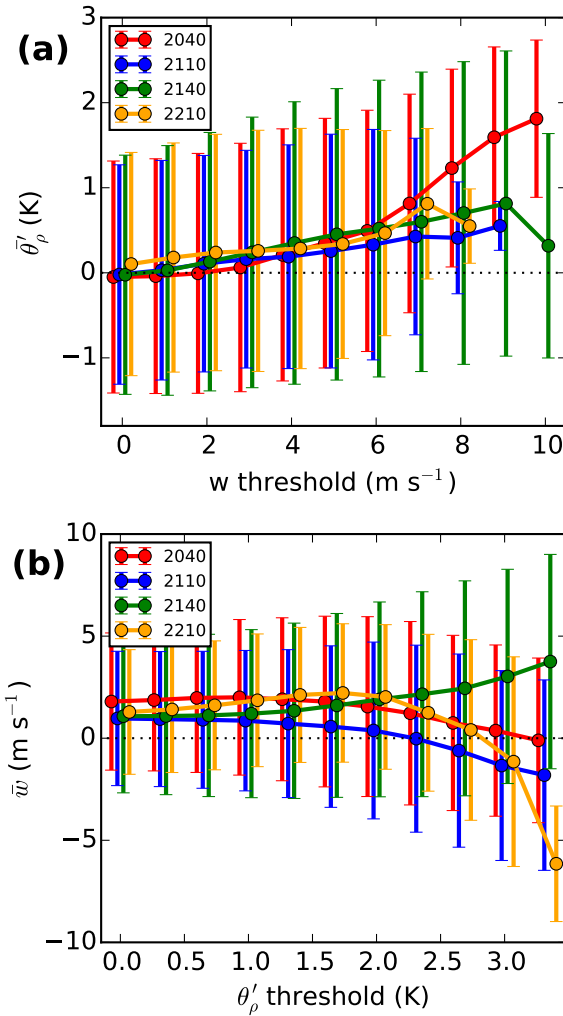


FIG. 13. (a)Unbalanced  $\theta'_\rho$  averaged over all gridpoints in the left-of-shear quadrants that exceed a certain vertical velocity threshold for 2040 UTC (red), 2110 UTC (blue), 2140 UTC (green), and 2210 UTC (orange). (b) Vertical velocity averaged over all gridpoints in the downshear quadrants that exceed a certain unbalanced  $\theta'_\rho$  threshold. Vertical errorbars indicate standard deviations.

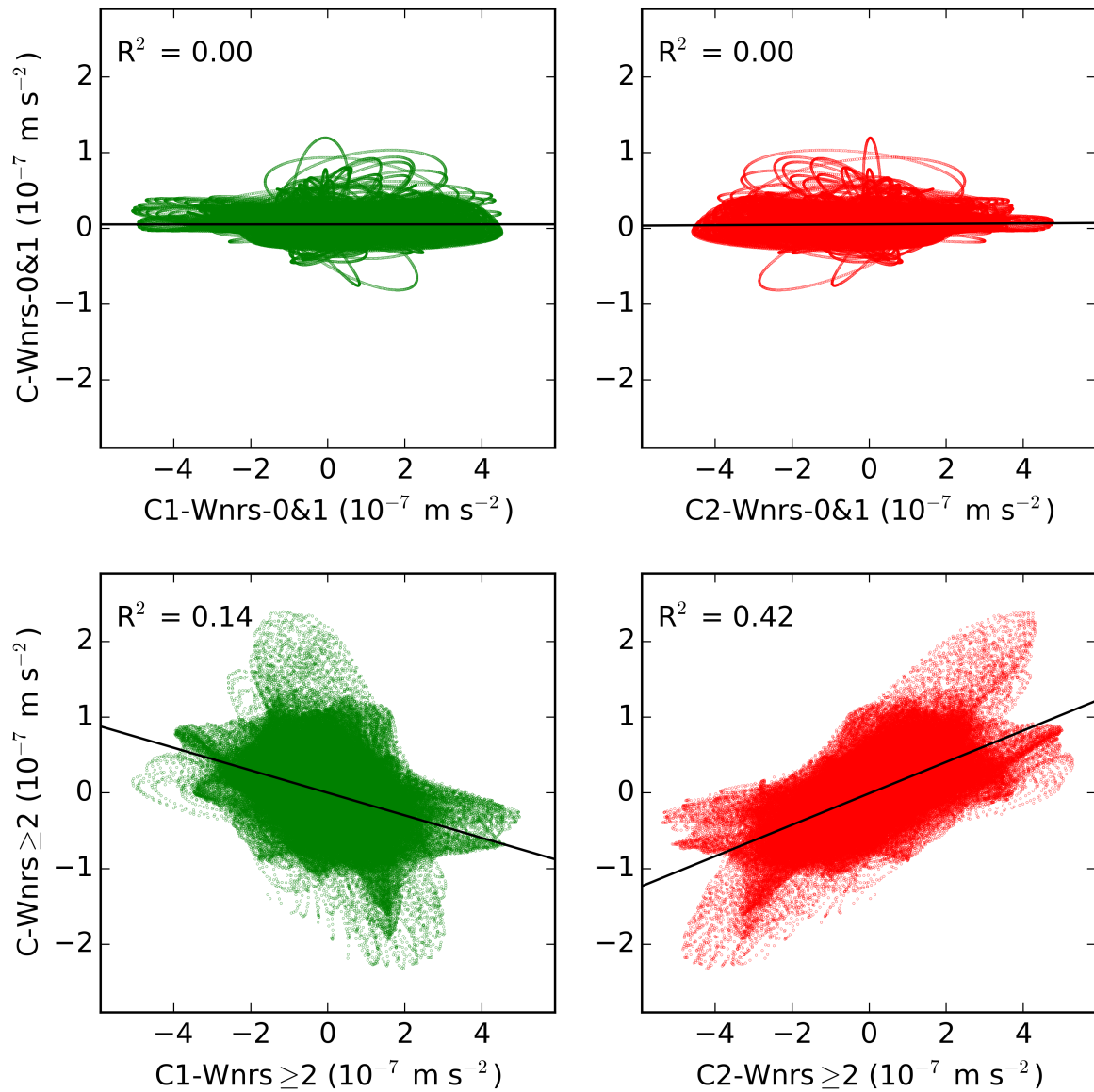


FIG. 14. Scatter plots of vertical acceleration (C), dynamic forcing (C1), and thermodynamic forcing (C2) for wavenumbers 0-and-1, and wavenumbers 2-and-higher. The scatter plots contain data of the eyewall region ( $15 \text{ km} \leq r \leq 40 \text{ km}$ ,  $2 \text{ km} \leq z \leq 8 \text{ km}$ ) of all four periods.

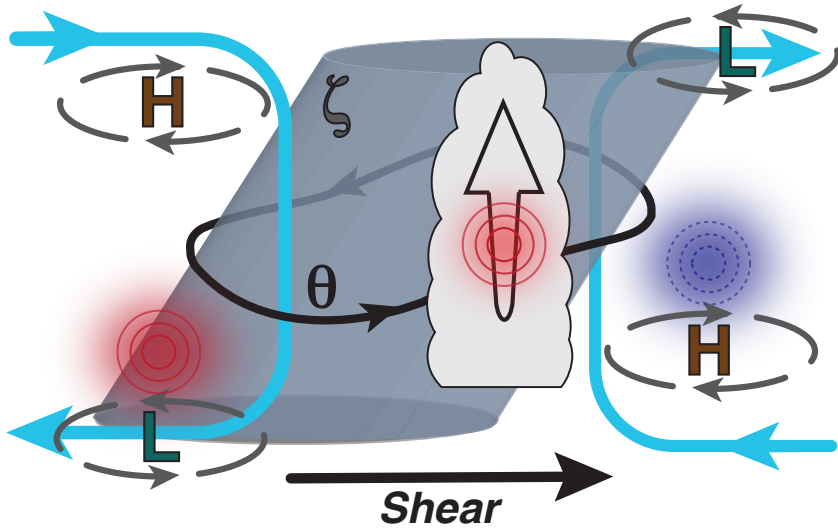


FIG. 15. Summary schematic of the kinematic and thermodynamic structure of Hurricane Rita (2005). The gray cylinder represents the vortex tower of the eyewall, which is tilted by the environmental wind shear (black vector). Green 'L' symbols and vectors denote cyclonic low pressure anomalies, and brown 'H' symbols denote anticyclonic high pressure anomalies. Thermal anomalies are denoted by blue (cold) and red (warm) circles and shading. Blue arrows show the modified secondary circulation. The thick black contour denotes a representative potential temperature surface, with arrows illustrating the cyclonic vortex flow around the eyewall. In the downshear right quadrant, air parcels move cyclonically downstream and adiabatically upward along the potential temperature surface resulting in individual convective motions denoted by the cumulus cloud and upward arrow. A warm anomaly is shown in the convective cloud to denote the release of latent heat associated with the buoyant updraft.